nature communications

Article

https://doi.org/10.1038/s41467-025-60586-8

Bioactive lipid mediator class switching regulates myogenic cell progression and muscle regeneration

Received: 13 June 2024

Accepted: 28 May 2025

Published online: 01 July 2025

Check for updates

Paul Fabre[1,2], Thomas Molina[1,2], Jessica Larose[3], Karine Greffard[3], Gregory Généreux-Gamache[1,4], Alyson Deprez[1,2], Inès Mokhtari[1,2], Ornella Pellerito[1], Elise Duchesne[5,6,7,8], Junio Dort[9], Jean-François Bilodeau[3,10] & Nicolas A. Dumont[1,4]

The muscle stem cell niche is well-described as influencing myogenic cell fate decision; however, the intrinsic mechanisms driving muscle stem cell progression during myogenesis are not yet fully elucidated. Here, we demonstrate that bioactive lipid class switching, an auto-regulatory mechanism originally described during the inflammatory process, is conserved during myogenesis. During the transition from proliferation to differentiation, myogenic cells shift from pro-inflammatory to pro-resolution pathways, a process partially mediated by 15Δ-PGJ_2 that promotes the expression of the prostaglandin inactivation enzyme 15-hydroxyprostaglandin dehydrogenase. Using pharmacological inhibitors and knockout models of the pro-resolution enzyme 15-lipoxygenase, we show that blocking the bioactive lipid class switching impairs myoblast differentiation in vitro and muscle regeneration in vivo. Administration of the pro-resolving mediator Protectin-D1 restores myogenesis, enhances muscle regeneration post-injury and improves muscle phenotype in a dystrophic mouse model. Overall, these findings provide a better comprehension of the mechanisms regulating myogenic progression, which opens new therapeutic avenues for muscle regeneration and dystrophies.

Skeletal muscle growth and regeneration are ensured by muscle stem cells (MuSCs) through a highly regulated process termed myogenesis[1,2]. After an injury, the quiescent MuSCs are activated and enter the cell cycle to become proliferating myoblasts[3]. After an expansion period, myoblasts exit the cell cycle either to self-renew and maintain the MuSC pool, or to differentiate and fuse to form myotubes which mature into myofibers[4].

Different cell types in the MuSC microenvironment, such as inflammatory cells and fibro-adipogenic progenitors, were shown to intervene in the muscle regeneration process to regulate myogenic cell fate decision[5,6]. For instance, during the early phase of muscle regeneration, pro-inflammatory macrophages and T cells were shown to release pro-inflammatory cytokines, such as TNF-α, IL-1, and IL-6,

[1]CHU Sainte-Justine Research Center, Montreal, QC, Canada. [2]Department of pharmacology and physiology, Faculty of Medicine, Université de Montréal, Montréal, QC, Canada. [3]Endocrinology and Nephrology Unit, CHU de Québec-Laval University Research Center, Québec, QC, Canada. [4]School of Rehabilitation, Faculty of Medicine, Université de Montréal, Montréal, QC, Canada. [5]School of Rehabilitation Sciences, Faculty of Medicine, Université Laval, Quebec, QC, Canada. [6]CHU de Québec - Université Laval Research Center, Quebec, QC, Canada. [7]Groupe de Recherche Interdisciplinaire sur les Maladies Neuromusculaires (GRIMN), Centre Intégré Universitaire de Santé et de Services Sociaux du Saguenay-Lac-Saint-Jean, Saguenay, QC, Canada. [8]Centre Interdisciplinaire de Recherche en Réadaptation et Intégration Sociale (Cirris), Centre Intégré Universitaire de Santé et de Services Sociaux Capitale-Nationale, Quebec, QC, Canada. [9]School of Pharmaceutical Sciences, Faculty of Medicine, University of Ottawa, Ottawa, ON, Canada. [10]Department of Medicine, Faculty of Medicine, Université Laval, Quebec, QC, Canada. e-mail: nicolas.dumont.1@umontreal.ca

promoting myoblasts proliferation[7,8], whereas anti-inflammatory macrophages and Tregs involved in the later phase of acute injury secrete cytokines/growth factors promoting myoblasts differentiation and fusion (e.g., IL-4, IGF-1)[9,10].

Specialized pro-resolving mediators (SPMs) have emerged as a new class of key regulators of inflammation[11–14]. These mediators are derived from poly-unsaturated fatty acids (PUFAs) such as arachidonic acid (AA, 20:4, ω−6), eicosapentaenoic acid (EPA, 20:5, ω−3), and docosahexaenoic acid (DHA, 22:6, ω−3). During the onset phase of acute inflammation, PUFAs are initially converted into pro-inflammatory bioactive lipids (e.g., prostaglandins, leukotrienes) during the first few hours or days post-injury (dpi)[11]. Thereafter, pro-resolving bioactive lipids such as Lipoxins, Protectins, Maresins, Resolvin-D series (derived from DHA), and Resolvin-E series (derived from EPA) increase to dampen the inflammatory process. This mechanism is mediated by an auto-regulatory feedback loop, called lipid mediator class switching, during which the pro-inflammatory enzymes cyclooxygenase-2 (COX-2) or 5-lipoxygenase (Alox5) are substituted by the pro-resolving enzymes, 12- and 15- lipoxygenases (Alox12, Alox15). In immune cells, this switch was shown to be mediated by the secretion of high levels of prostaglandin-E2 (PGE_2), which triggers the reduction in Alox5 expression and increases in the expression of Alox15[11].

Bioactive lipids mediate their immunomodulatory effects by binding to specific G-protein coupled receptors (GPCRs). For instance pro-inflammatory lipids, such as PGE_2, bind to GPCRs such as EP1-4 expressed by different cell types to induce vasodilation, vascular leakage, and leukocyte recruitment[15]. Alternatively, pro-resolving lipid mediators target GPCRs such as ALX/FPR2 (lipoxin-A4 receptor), ChemR23/Cmklr1 (Resolvin-E receptor), or GPR37 (Protectin D1 receptor) to reduce pro-inflammatory cytokine secretion, limit leukocyte infiltration, enhance the clearance of apoptotic cells, and promote macrophage shift to their pro-resolving phenotype, which are important steps in the return to homeostasis[16]. In addition to targeting inflammatory cells such as macrophages, neutrophils, and dendritic cells, these bioactive lipids were also shown to affect tissue-resident cells like epithelial cells, endothelial cells, fibroblasts, and smooth muscle cells to regulate their migration, proliferation, and paracrine secretion to stimulate regeneration[17]. Accordingly, pro-resolving lipids showed promising therapeutic potential in different immune-related conditions such as periodontal disease[18,19], sepsis[20], bacterial infection[21,22], Alzheimer's disease[23], Parkinson's disease[24], cystic fibrosis[25], and others[26].

Despite their key roles in many pathophysiological processes, the impact of bioactive lipids on skeletal muscle biology has been poorly investigated. Recently, it has been shown that muscle injuries induced by cardiotoxin or eccentric exercise trigger a rapid increase in pro-inflammatory lipids in the muscle in the first 24–48 h post-injury, which is followed by an increased expression of pro-resolving lipids[27]. Pioneer studies showed that PGE_2 targets one of its 4 receptors, the EP4 receptor, on MuSCs to stimulate their cell cycle entry and the rate of cell proliferation, in particular symmetric self-renewal[28,29]. Alternatively, Resolvin-D1 was shown to have a potential immunomodulating effects on MuSCs and have a modest effect on myoblast fusion[30]. Our recent findings also indicate that Resolvin-D2 can directly stimulate myoblast differentiation by targeting the Gpr18 receptor, which enhances muscle regeneration in a mouse model of Duchenne Muscular Dystrophy (DMD)[31]. This emerging body of literature suggests that bioactive lipids are modulators of skeletal muscle regeneration; however, the impact of the bioactive lipids on the intrinsic regulation of MuSCs fate decision during myogenesis is still unknown.

Using transcriptomics and lipidomic targeted analyses, we showed in this study that there is a rapid switch in bioactive lipid profile in favor of pro-resolving mediators that happens when proliferating myoblasts exit the cell cycle to differentiate. The blockade of this bioactive lipid class switch compromised myoblast differentiation in vitro and muscle regeneration in vivo, which can be rescued by the administration of the pro-resolution lipid mediator Protectin D1 (PD1). Furthermore, PD1 treatment ameliorates the muscle phenotype and function in a model of DMD. Overall, our findings indicate that the bioactive lipid class switching is not exclusive to immune cells and is conserved in myogenic cells where it plays a role in regulating cell fate decision during myogenesis. These findings open the way for the development of new therapeutic avenues for muscular dystrophies in which muscle regenerative capacities are compromised.

Results

Pro-inflammatory enzyme expression drops during myogenesis

To assess the changes in bioactive lipid profile during myogenesis, primary MuSCs were isolated by FACS (Supplementary Fig. 1) from wildtype mice and cultured in vitro in proliferating medium, or in differentiating medium for 1, 2, 3, 4, or 5 days (Fig. 1a). Analysis of RNA and protein expression revealed a reduction in the pro-inflammatory enzymes associated with the AA pathway during the entry of myogenic cells into differentiation. Specifically, regarding the leukotriene biosynthesis pathway (Fig. 1b), we showed that the expression of *Alox5* is drastically reduced at the RNA level at the initiation of differentiation, which is gradually followed by a reduction at the protein level (Fig. 1c, d). The expression of *Alox5AP* (*Alox5 activating protein*), a key enzyme needed for Alox5 to produce leukotrienes, is also reduced during differentiation (Fig. 1e). Alox5 and Alox5AP can metabolize AA into leukotriene-A4 (LTA_4), which is then converted into Leukotriene-B_4, -C_4, -D_4, or -E_4 by the enzymes LTA_4 Hydrolase (LTA4H), LTC_4 Synthase (LTC4S), or microsomal glutathione S-transferase 2 (MGST2), respectively. All these downstream enzymes were also downregulated during myoblast differentiation in vitro (Fig. 1f–h).

Regarding the prostaglandin pathway (Fig. 1i), our findings demonstrate a rapid reduction of *Ptgs2* expression (Prostaglandin-endoperoxide synthase, gene encoding for COX-2), and a consequent decrease in the protein COX-2 during differentiation (Fig. 1j, k). COX-2 converts AA into prostaglandin-H2 (PGH_2), which is then metabolized into PGD_2, PGE_2, PGI_2, or thromboxane-A_2 (TXA_2), by the enzymes prostaglandin-D2 synthase (*Ptgds*), PGE synthase (*Ptges*), prostaglandin-I2 synthase (*Ptgis*), and thromboxane-A synthase 1 (*Tbxas1*), respectively. The expression of the enzymes *Tbxas1*, *Ptgis*, and *Ptges* is not significantly changed during differentiation (Fig. 1l–n). However, *Ptgds* expression showed a strong increase (~50–60 fold) during differentiation (Fig. 1o). This enzyme is responsible for the synthesis of the PGD_2, which is then converted into Prostaglandin J2 (PGJ_2) and 15-deoxy-prostaglandin J2 (15Δ-PGJ_2)[32].

Pro-resolving enzyme expression increases during myogenesis

To further characterize the bioactive lipid class switching, we investigated if the myogenic progression from proliferation to differentiation was associated with changes in pro-resolving enzyme expression (Fig. 2a). We first observed that the expression of *Pla2g2d* (phospholipase 2 group IID), an enzyme identified as a"resolving sPLA2" by its ability to preferentially biosynthesize omega-3 PUFAs EPA and DHA, and AA-derived anti-inflammatory prostanoids PGD_2 and 15Δ-PGJ_2[33], is increased during myogenic cell differentiation (Fig. 2b). The expression of the pro-resolution enzymes *Alox15* and *Alox12* involved in the oxidation of EPA and DHA into pro-resolving lipids is also increased during myogenic cell differentiation (Fig. 2c–e). *Alox15* expression displays a sharp increase from the first day of differentiation at the RNA and protein level, whereas the increase in *Alox12* expression happens gradually and peaks later during the differentiation process (days 3–5). Finally, our findings showed a gradual increase in the expression of *Hpgd*, which encodes for the enzyme 15-hydroxyprostaglandin dehydrogenase (15-PGDH) that is responsible for the degradation of different prostaglandins (e.g., PGE_2, $PGF_{2\alpha}$, PGI_2) (Fig. 2f)[34]. Altogether,

https://doi.org/10.1038/s41467-025-60586-8

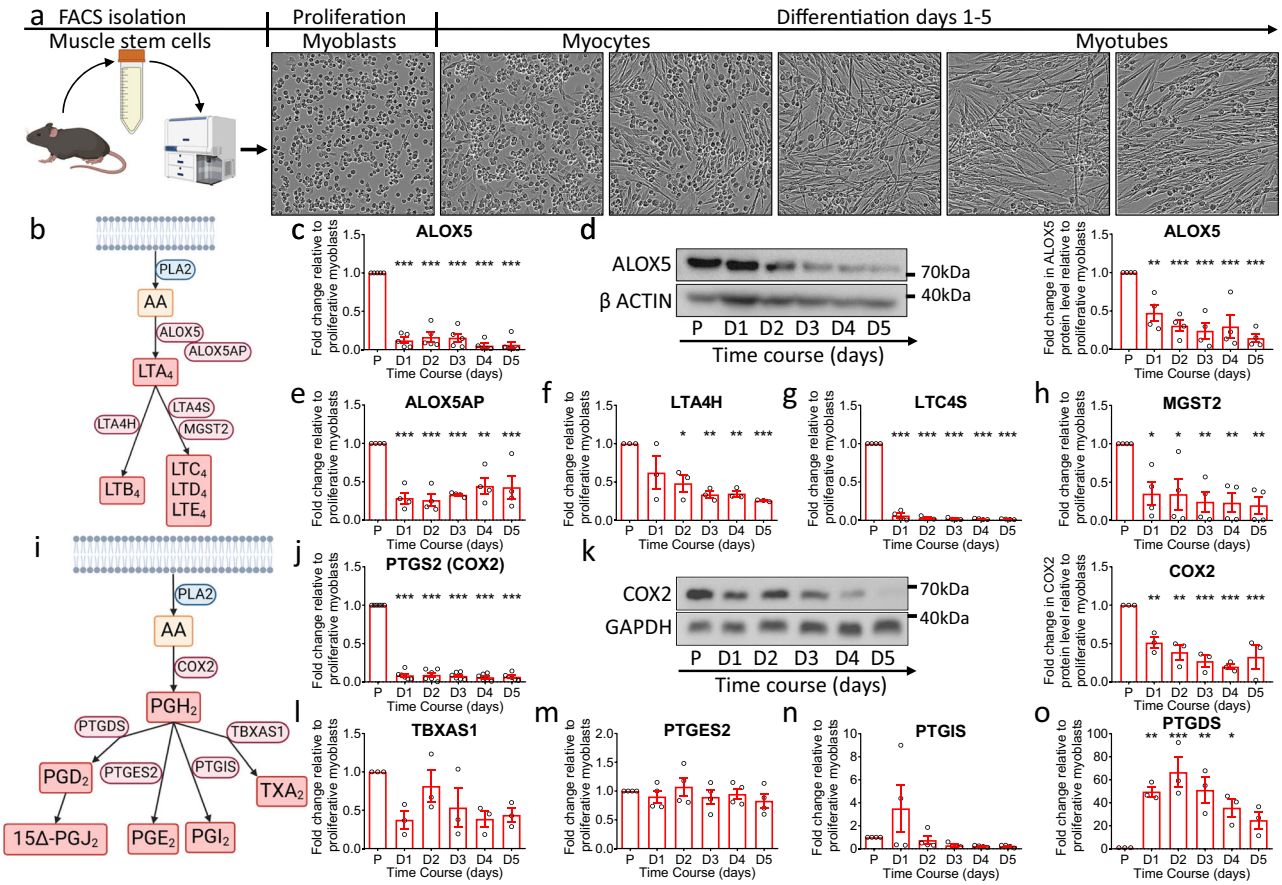


Fig. 1 | Reduction in pro-inflammatory bioactive lipid biosynthesizing enzymes during myogenic progression. a Graphical overview of the myoblast isolation, culture, and differentiation experiment (Created in BioRender)[88]. **b** Graphical representation of the leukotriene synthesis cascade (Created in BioRender)[89]. **c**–**h** Expression of leukotriene synthesis enzymes quantified by qPCR: *Alox5* (**c**) (P vs. D1 $p < 0.0001$; P vs. D2 $p < 0.0001$; P vs. D3 $p < 0.0001$; P vs. D4 $p < 0.0001$; P vs. D5 $p < 0.0001$), *Alox5ap* (**e**) (P vs. D1 $p < 0.0001$; P vs. D2 $p < 0.0001$; P vs. D3 $p = 0.0002$; P vs. D4 $p = 0.0012$; P vs. D5 $p < 0.0009$), *Lta4h* (**f**) (P vs. D2 $p = 0.0133$; P vs. D3 $p = 0.0023$; P vs. D4 $p = 0.0026$; P vs. D5 $p = 0.0009$), *Ltc4s* (**g**) (P vs. D1 $p < 0.0001$; P vs. D2 $p < 0.0001$; P vs. D3 $p < 0.0001$; P vs. D4 $p < 0.0001$; P vs. D5 $p < 0.0001$), *Mgst2* (**h**) (P vs. D1 $p = 0.0124$; P vs. D2 $p = 0.0116$; P vs. D3 $p = 0.0038$; P vs. D4 $p = 0.0033$; P vs. D5 $p = 0.0022$). **d, k** Representative Western Blots and quantification of the enzymes ALOX5 (**d**) (P vs. D1 $p = 0.0045$; P vs. D2 $p = 0.0003$; P vs. D3 $p = 0.0001$; P vs. D4 $p = 0.0003$; P vs. D5 $p < 0.0001$) and COX-2 (**k**) (P vs. D1 $p = 0.0073$; P vs. D2 $p = 0.0013$; P vs. D3 $p = 0.0003$; P vs. D4 $p = 0.0001$; P vs. D5 $p = 0.0006$) expression during myogenesis (relative to GAPDH or β-actin as loading control). **i** Graphical representation of the prostaglandin synthesis cascade (Created in BioRender)[89]. **j**, **l**–**o** Expression of prostaglandin synthesis enzymes quantified by qPCR: *Ptgs2* (**j**) (P vs. D1 $p < 0.0001$; P vs. D2 $p < 0.0001$; P vs. D3 $p < 0.0001$; P vs. D4 $p < 0.0001$; P vs. D5 $p < 0.0001$), *Tbxas1* (**l**), *Ptges2* (**m**), *Ptgis* (**n**), *Ptgds* (**o**) (P vs. D1 $p = 0.0061$; P vs. D2 $p = 0.0006$; P vs. D3 $p = 0.0050$; P vs. D4 $p = 0.0489$). Results are expressed as mean +/- SEM. Biological replicates $n = 5$ for panel **c**; $n = 4$ for panels **d, e, g, h, m, n**; $n = 6$ for panel **j**; $n = 3$ for panels **f, k, l, o**. $^{*}p < 0.05$, $^{**}p < 0.01$, $^{***}p < 0.001$. One-Way ANOVA with Dunnett's multiple comparisons test. Source data are provided as a Source Data file.

these findings indicate that there is a bioactive lipid class switching characterized by a reduction in the pro-inflammatory lipid enzymes and an increase in the pro-resolving lipid enzymes when myogenic cells exit the cell cycle to differentiate.

Next, to explore the cause of that enzymatic switching, we tested the effect of PGE_2 supplementation on myogenic cells, since this bioactive lipid was previously shown to trigger the bioactive lipid class switch in immune cells[11]. However, administration of PGE_2 on myogenic cells increased the expression of *Ptgs2* (COX-2), *Alox5*, *Alox5ap*, and *Ptger4* (EP4 receptor), and reduced the expression of *Hpgd* (15-PGDH), which would result in a positive feedback loop enhancing pro-inflammatory lipid production (Fig. 2g, h, and Supplementary Fig. 2a–c). Accordingly, treatment of myoblasts with PGE_2 increased cell proliferation (Supplementary Fig. 2d). Next, since *Ptgds* is the only enzyme involved in the AA pathway that increases during differentiation (Fig. 1o), we investigated if the downstream bioactive lipids, PGD_2 or $15\Delta\text{-}PGJ_2$, could mediate the enzymatic switch. The administration of $15\Delta\text{-}PGJ_2$ significantly increased the expression of *Hpgd* (Fig. 2h). To determine if this mechanism is also observed in vivo, we investigated the expression of these different prostaglandin synthesis enzymes in a publicly available dataset that performed single cell RNAseq (scRNAseq) at different time points post-cardiotoxin injury (uninjured, 0.5, 2, 3.5, 5, 10, 21 dpi)[35]. By analyzing the myogenic cell subpopulation, we observed that *Ptgs2* and *Ptges* expression peaks at 2 dpi, while *Ptgds* and *Hpgd* expression rises later at 3.5 dpi, a time point at which myogenic differentiation increases drastically as shown by *Myog* expression (Fig. 2i). Subsequent analysis of the cell types expressing *Ptgds* at 3.5 dpi revealed that 20.73% of the Pax7 + /MyoD- MuSC express *Ptgds*, whereas this proportion increases by >2-fold to 45.05% and 46.88% in Pax7-/MyoD+ cell population and Myog+ cell subsets, respectively (Fig. 2j). These findings suggest that our in vitro observations showing a change in bioactive lipid profile when myogenic cells enter differentiation are also reflected, to a degree, in regenerating muscle in vivo. Altogether, these findings suggest that the switch in bioactive lipid biosynthesizing enzymes initially described in the inflammatory cells is also occurring in myogenic cells during myogenesis.

https://doi.org/10.1038/s41467-025-60586-8

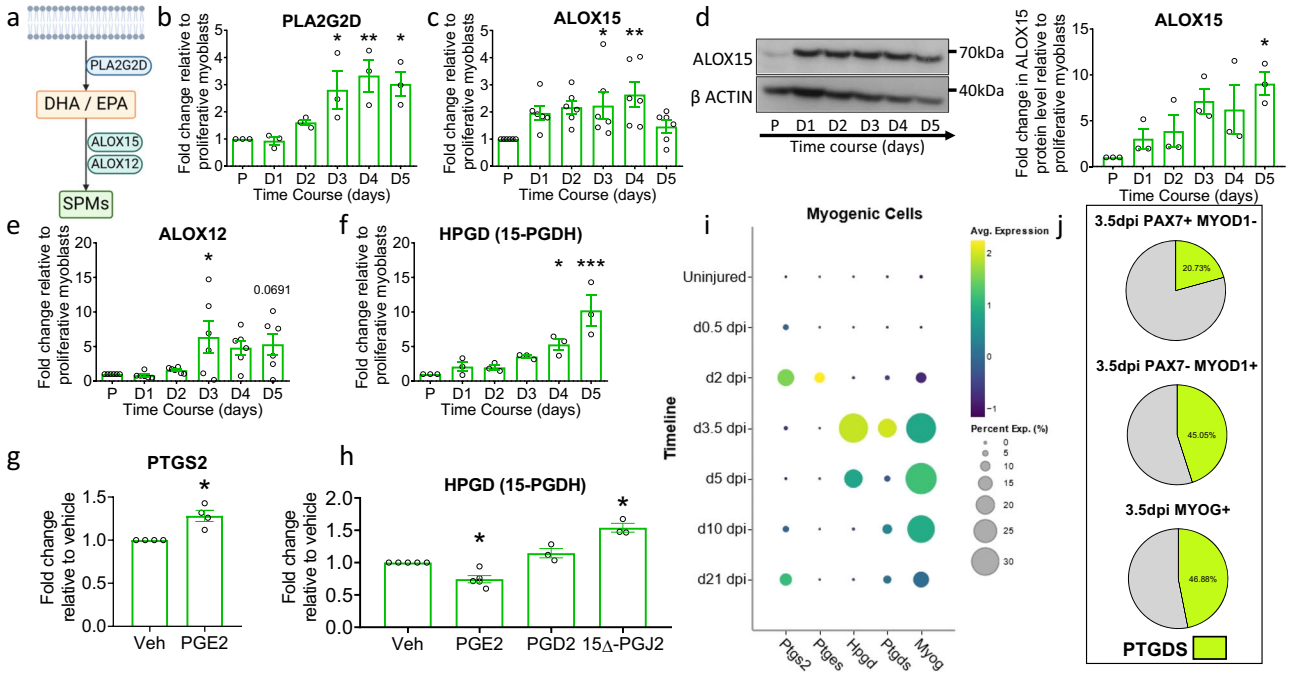


Fig. 2 | Increase in pro-resolving lipid biosynthesizing enzymes during myogenic progression. a Graphical representation of the pro-resolving lipid mediator cascade (Created in BioRender)[90]. **b, c, e** Expression of pro-resolving enzymes quantified by qPCR: *Pla2g2d* (**b**) (P vs. D3 $p = 0.0413$; P vs. D4 $p = 0.0088$; P vs. D5 $p = 0.0218$), *Alox15* (**c**) (P vs. D3 $p = 0.0487$; P vs. D4 $p = 0.0057$) and *Alox12* (**e**) (P vs. D3 $p = 0.0169$). **d** Representative Western Blots and quantification of the enzyme ALOX15 during myogenesis (relative to β-actin as loading control) (P vs. D5 $p = 0.0133$). **f** Expression of the prostaglandin-degrading enzyme *Hpgd* quantified by qPCR (P vs. D4 $p = 0.0430$; P vs. D5 $p = 0.0002$). **g** Expression of *Ptgs2* after 24 h treatment with prostaglandins PGE_2 (250 nM) or vehicle ($p = 0.0221$). **h** Expression of *Hpgd* after 24 h treatment with prostaglandins PGE_2 (250 nM), PGD_2 (250 nM) and 15Δ-PGJ_2 (250 nM) (Veh vs PGE2 $p = 0.0103$; Veh vs 15Δ-PGJ2 $p = 0.0155$). **i** Expression of *Ptgs2*, *Ptges*, *Hpgd*, *Ptgds*, and *Myog* from single cell RNA sequencing dataset (Oprescu SN et al. iScience 2020) from uninjured, 0.5, 2, 3.5, 5, 10, and 21 days post-injury (dpi) in WT muscle. **j** Proportion of cells expressing *Ptgds* in MuSCs (Pax7+MyoD-), myoblasts (Pax7-MyoD +), or differentiated myoblasts (Pax7-Myog +) in WT muscle at 3.5 dpi (Oprescu SN et al. iScience 2020). Results are expressed as mean +/- SEM. Biological replicates $n = 3$ for panels **b, d, f**; $n = 6$ for panels **c**, **e**; $n = 4$ for panel **g**; $n = 5$ for panel h (except $n = 3$ for PGD_2 and 15Δ-PGJ_2 groups). *$p < 0.05$, **$p < 0.01$, *** $p < 0.001$. 2-way Paired t-test (**g, h**), One-way ANOVA with Dunnett's multiple comparisons test (**b, c, d, e, f**). Source data are provided as a Source Data file.

A bioactive lipid class switching occurs during myogenesis

We next evaluated the expression of bioactive lipids and their receptors during myogenesis in vitro to determine if they follow the same expression pattern as their biosynthesizing enzymes. Targeted mass spectrometry lipidomic analyses were performed on the conditioned medium of proliferating myoblasts and differentiating myocytes (after 1, 3, 5 days of differentiation) to assess their secretion of bioactive lipids. We observed that the lipid profile drastically changes during myogenesis in vitro (Fig. 3a–q). Regarding the AA cascade, the levels of the proinflammatory lipid mediators prostaglandin $F_{2\alpha}$ ($PGF_{2\alpha}$), PGE_2, and Thromboxane B_2 (TXB_2) – a stable metabolite of TXA_2 – showed a rapid and sustained decrease during differentiation (Fig. 3b–d). PGD_2 is the only COX2-derived lipid mediator that showed an increasing, but non-significant, pattern during differentiation (Fig. 3e).

For the pro-resolving mediators, the AA-derived Lipoxin A_4 (LXA_4) and 15(*R*)-LXA_4 increase during differentiation (Fig. 3j, and Supplementary Fig. 3a). For the EPA cascade, the pro-resolving lipid Resolvin E_1 (RvE1) does not show significant variation across differentiation (Fig. 3k). For the DHA cascade, the level of Resolvin D5 $_{n\text{-}3\ DPA}$ (RVD5 $_{n\text{-}3\ DPA}$) is rapidly increasing during myogenic differentiation, and protectin-DX (PDX) showed a similar trend (Fig. 3l, m).

Next, we assessed the expression of the bioactive lipid receptors during myogenic progression. The expression of the pro-inflammatory lipid receptors prostaglandin E2 receptor 4 (EP4) and prostaglandin F receptor (*Ptgfr*) is reduced during differentiation, while the thromboxane Receptor (TP; *Tbxa2r* gene) expression is not significantly changed (Fig. 3f–h). On the other hand, the PGD_2/15Δ-PGJ_2 receptor DP2 showed an increase in its expression during differentiation, which is consistent with its role in promoting bioactive class switching (Fig. 3i). Regarding the expression of pro-resolving lipid receptors, lipoxin-A_4 and 15(R)-LXA_4 can target two receptors, N-formyl peptide receptor 2 (*Fpr2*), which decreases during differentiation, and aryl hydrocarbon receptor (*Ahr*) that is non-significantly changed during differentiation (Fig. 3n, Supplementary Fig. 3b). Other pro-resolving receptors, such as the Resolvin-E1 receptor (*Cmklr1*) showed a non-significant trend toward increased expression, while $RvD5_{n\text{-}3\ DPA}$ receptor G-protein coupled receptor 101 (*Gpr101*) is reduced during differentiation (Fig. 3o, p). Noteworthy, the protectin receptor G-protein coupled receptor 37 (*Gpr37*) increases by up to 9-fold during differentiation (Fig. 3q). Altogether, these data reveal that there is a switch in bioactive lipid expression from pro-inflammatory to pro-resolving mediators during myogenic cell differentiation; however, the expression of their respective receptors does not necessarily correlate with the expression of the ligand.

Alox15 plays a key role in the regulation of myogenesis

To assess the impact of bioactive lipid class switching on myogenesis, we isolated MuSCs from B6.129S2-Alox15^{tm1Fun}/J mice (*Alox12/15*-knockout mice, hereafter called *Alox15*-KO) and their wild-type littermates (WT). Using targeted lipidomic analysis, we first assessed the levels of bioactive lipids on the conditioned medium of *Alox15*-KO compared to control myogenic cells during myogenesis in vitro (Fig. 4a–h). This analysis revealed that the reduction in COX-2-derived pro-inflammatory mediators such as PGE_2, PGF_{2a}, and TXB_2, observed during myogenic differentiation is not affected by the lack of *Alox15* (Fig. 4a–c). Intriguingly, the increasing trend observed for PGD_2 during

https://doi.org/10.1038/s41467-025-60586-8

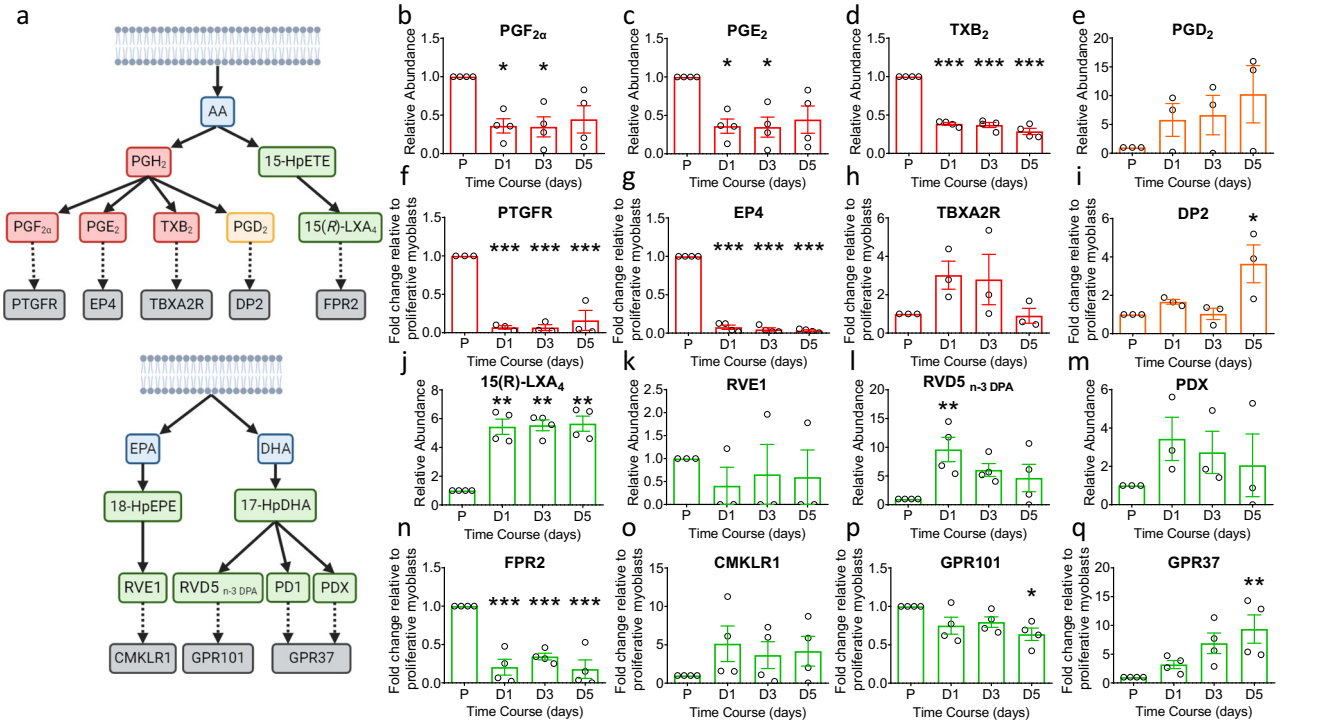


Fig. 3 | Targeted lipidomics identifies the bioactive lipid class switching from pro-inflammatory lipids to pro-resolving lipids during myogenic progression. **a** Graphical representation of the pro-inflammatory and pro-resolving lipid mediator cascade (green). Bioactive lipid receptors are identified in gray boxes. (Created in BioRender)[91]. **b**–**e**, **j**–**m** Quantification by mass spectrometry (LC-MS/MS) of lipid mediator levels measured in the medium of proliferating vs differentiating myoblasts (day 1, 3, 5): PGF_{2a} (**b**) (P vs. D1 $p = 0.0134$; P vs. D3 $p = 0.0329$), PGE_2 (**c**) (P vs. D1 $p = 0.0134$; P vs. D3 $p = 0.0329$), TXB_2 (**d**) (P vs. D1 $p = 0.0001$; P vs. D3 $p = 0.0007$; P vs. D5 $p = 0.0009$), PGD_2 (**e**), 15(R)-LXA_4 (**j**) (P vs. D1 $p = 0.0076$; P vs. D3 $p = 0.0027$; P vs. D5 $p = 0.0065$), RvE1 (**k**), $RvD5_{n\text{-}3\ DPA}$ (**l**) (P vs. D1 $p = 0.0096$), PDX (**m**). **f**–**i**,**n**–**q** Quantification by qPCR of bioactive lipid receptors' expression in myogenic cells during myogenesis in vitro: *Ptgfr* (**f**) (P vs. D1 $p < 0.0001$; P vs. D3 $p < 0.0001$; P vs. D5 $p < 0.0001$), *EP4* (**g**) (P vs. D1 $p < 0.0001$; P vs. D3 $p < 0.0001$; P vs. D5 $p < 0.0001$), *Tbxa2r* (**h**), *DP2* (**i**) (P vs. D5 $p = 0.0176$), *Fpr2* (**n**) (P vs. D1 $p < 0.0001$; P vs. D3 $p = 0.0003$; P vs. D5 $p < 0.0001$), *Cmklr1* (**o**), *Gpr101* (**p**) (P vs. D5 $p = 0.0150$), *Gpr37* (**q**) (P vs. D5 $p = 0.0068$). **a**–**q** Pro-inflammatory lipids and receptors are identified in red, pro-resolving lipids and receptors are identified in green, and PGD_2/DP2 that play a role in triggering the switch are identified in orange. Results are expressed as mean +/- SEM. Biological replicates $n = 4$ for panels **b**–**d, g, j, l, n**–**q**; $n = 3$ for panels **e, f, h, i, k, m**. $^*p < 0.05$, $^{**}p < 0.01$, $^{***}p < 0.001$. Repeated measure one-way ANOVA with Dunnett's multiple comparisons test (**b**–**e, j**–**m**), One-way ANOVA with Dunnett's multiple comparisons test (**f**–**i**, **n**–**q**). Source data are provided as a Source Data file.

the differentiation of WT myogenic cells is not observed in absence of *Alox12/15* (Fig. 4d). Alternatively, the expression of pro-resolving lipid mediators is affected in *Alox15*-KO cells compared to WT myogenic cells. The increase in the expression of pro-resolving mediators such as LXA_4, 15(*R*)-LXA_4, $RvD5_{n\text{-}3\ DPA}$, and PDX, which was observed during WT cell differentiation is not happening in the *Alox15*-KO cells, which maintain a low basal level throughout differentiation (Fig. 4e–h). Altogether, these results indicate that bioactive lipid class switching is impaired in the absence of *Alox15*.

Next, we investigated if this impairment in the bioactive lipid profile in *Alox15*-KO was affecting myogenic cell behavior in vitro. When the myoblasts are maintained in proliferative conditions, the growth rate is similar between *Alox15*-KO and WT cells (Fig. 4i). Moreover, immunostaining performed on *Alox15*-KO myoblasts seeded at low confluence and cultured in the proliferating medium for 4–5 days demonstrated a high ratio of Pax7+ cells (proliferating myoblasts) and a low ratio of Myog+ cells (differentiated myoblasts) that is similar to the one observed in WT cells (Fig. 4j-l). Alternatively, *Alox15*-KO cells showed a different behavior than WT cells when pushed toward differentiation in the low-serum medium. Immunostaining revealed that there is a higher proportion of *Alox15*-KO cells that express Pax7 and MyoD and a lower percentage of cells that acquire Myog after 1 day of differentiation (Fig. 4m–p). Moreover, *Alox15*-KO myogenic cells showed a lower fusion index at 4 days of differentiation compared to WT (Fig. 4q). Altogether, these results suggest that in the absence of *Alox15*, the myogenic cells present a diminished ability to progress along the differentiation program.

ALOX15 regulates myogenesis of human myoblasts in vitro

To investigate the role of ALOX15 in human myogenesis, MuSCs were isolated from muscle biopsies (*vastus lateralis*) of healthy donors and cultured in vitro under proliferation or differentiation conditions for 3, 5, or 7 days (Fig. 5a–f). The expression dynamics of key enzymes involved in the bioactive lipid mediator pathways was assessed by qPCR. *ALOX5* level remained relatively stable throughout differentiation (Fig. 5a), whereas *ALOX5AP*, the binding partner regulating ALOX5 activity, exhibited a reduced expression as differentiation progressed (Fig. 5b). In the prostaglandin pathway, *PTGS2* expression also decreased during differentiation (Fig. 5c), while *PTGDS* displayed a 200–600-fold increase (Fig. 5d). Regarding the expression of pro-resolution enzymes, *ALOX15* displayed a rapid rise in the early days of differentiation, while *ALOX12* expression showed a non-significant increasing trend (Fig. 5e, f). *HPGD* expression was not significantly affected during the differentiation process (Supplementary Fig. 4a). The protectin receptor *GPR37* showed an increased expression during differentiation (Supplementary Fig. 4b).

Next, we examined whether a pharmacological inhibition of the *ALOX12/15* pathway could affect human myogenic cells behavior in vitro. Human myogenic cells cultured in proliferation and

https://doi.org/10.1038/s41467-025-60586-8

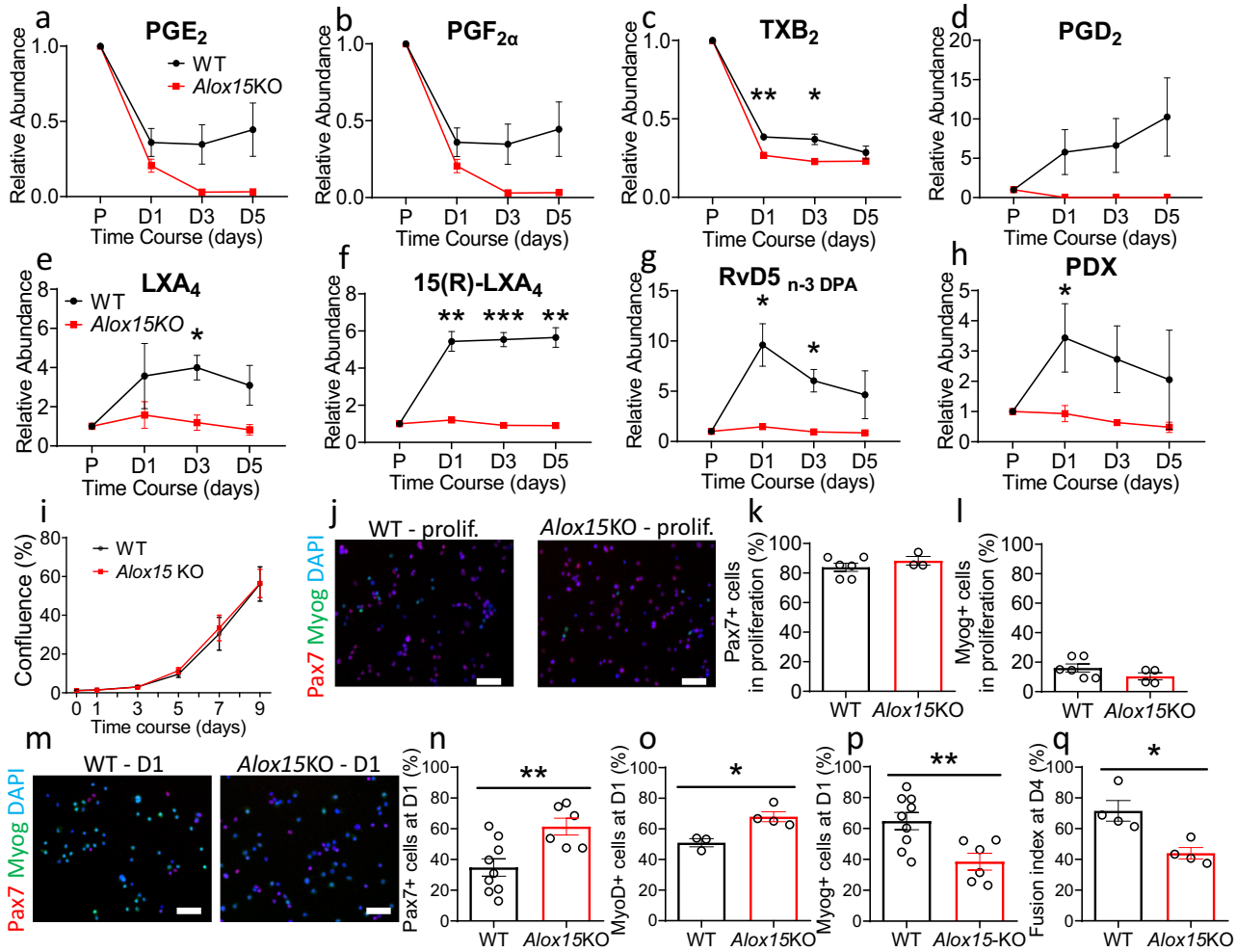


Fig. 4 | Lack of Alox15 impairs bioactive lipid class switching and blocks myogenic cell differentiation. a–h Quantification by mass spectrometry (LC-MS/MS) of bioactive lipid levels PGE_2 (**a**), $PGF2_a$ (**b**), TXB_2 (**c**) (P vs. D1 $p = 0.0066$; P vs. D3 $p = 0.0220$), PGD_2 (**d**), LXA_4 (**e**) (P vs. D3 $p = 0.0142$), 15(R)-LXA_4 (**f**) (P vs. D1 $p = 0.0029$; P vs. D3 $p = 0.0010$; P vs. D5 $p = 0.0020$), $RvD5_{n\text{-}3\ DPA}$ (**g**) (P vs. D1 $p = 0.0303$; P vs. D3 $p = 0.0185$), PDX (**h**) (P vs. D1 $p = 0.0447$) in the medium of wildtype (WT, black) and *Alox15*-knockout (*Alox15*-KO, red) myogenic cells during myogenesis. Results expressed as the fold change relative to proliferating myoblasts (asterisks indicate a significant difference in between *Alox15*-KO and WT at the same time point). **i** Growth curve of WT and *Alox15*-KO proliferating myoblasts. **j** Representative images of proliferating myoblasts immunostained for Pax7 (red), Myog (green), and DAPI (blue). Scale bars = 50 µm. **k, l** Quantification of the proportion of Pax7-expressing cells (MuSC/proliferative myoblasts) and Myog-expressing cells (differentiated myoblasts) in proliferating medium. **m** Representative images of differentiated myoblasts (day 1) immunostained for Pax7 (red), Myog (green), and DAPI (blue). Scale bars = 50 µm. **n–p** Quantification of the proportion of Pax7-expressing cells (MuSC/proliferative myoblasts) (**n**) ($p = 0.0067$), MyoD-expressing cells (committed myoblasts) (**o**) ($p = 0.0125$) and Myog-expressing cells (differentiated myoblasts) (**p**) ($p = 0.0070$) after 1 day in differentiation medium. **q** Fusion index of WT and *Alox15*-KO myogenic cells after 4 days in differentiation medium ($p = 0.0115$). Results are expressed as mean +/- SEM. Biological replicates $n = 4$ for WT and $n = 3$ for *Alox15*KO for panels (**a–c, e–g**); $n = 3$ for panels (**d**, **h**); $n = 5$ for panel (**i**); $n = 6$ for WT and $n = 3$ for *Alox15*KO for panel (**k**); $n = 6$ for WT and $n = 4$ for *Alox15*KO for panel (**l**); $n = 9$ for WT and $n = 6$ for *Alox15*KO for panels (**n**, **p**); $n = 3$ for WT and $n = 4$ for *Alox15*KO for panel (**o**); $n = 4$ for panel (**q**);. * $p < 0.05$, ** $p < 0.01$, *** $p < 0.001$. Repeated measures 2-way ANOVA with Uncorrected Fisher's LSD multiple comparisons test (**a–i**). 2 way Unpaired t-test (**k, l, n–q**). Source data are provided as a Source Data file.

differentiation conditions were treated with PD146176[36–38] or Baicalein[39,40] at concentrations of 10 µM or 20 µM for 3 days (Fig. 5g–i, Supplementary Fig. 5a, b). Under proliferative conditions, PD146176 did not significantly impact the growth rate of myogenic cells compared to vehicle controls (Fig. 5g). However, differentiating cells treated with PD146176 showed a dose-dependent reduction in the fusion index compared to the vehicle treated cells (Fig. 5h, i). Similar results were obtained with Baicalein that strongly blocked myogenic cell fusion, although it also mildly reduced cell proliferation (Supplementary Fig. 5a, b). Altogether, these results suggest that, similar to what was observed in mice, there is a bioactive lipid class switch during human myogenic cell progression in vitro, which plays a role in the differentiation process.

Alox15 expression regulates muscle regeneration in vivo

To investigate the impact of bioactive lipids in vivo, we assessed the skeletal muscle regenerative capacity in *Alox15*-KO mice (Fig. 6a). We first evaluated skeletal muscle composition in uninjured mice, and we observed no difference in the number of Pax7+ MuSCs and the size of the myofibers (minimal feret diameter; MFD) in *Alox15*-KO mice compared to controls (Fig. 6b–e).

Next, a cardiotoxin (CTX) injury was performed in the tibialis anterior (TA) muscle and muscle regeneration was assessed in the acute phase of regeneration at 7 dpi. We observed an increase in the number of Pax7+ cells but a reduction in Myog+ cells in *Alox15*-KO mice compared to WT (Fig. 6f–h). Moreover, the size of the myofibers was reduced in *Alox15*-KO muscles compared to the WT (Fig. 6i, j). Muscle regeneration was assessed later in the regenerative process during the

https://doi.org/10.1038/s41467-025-60586-8

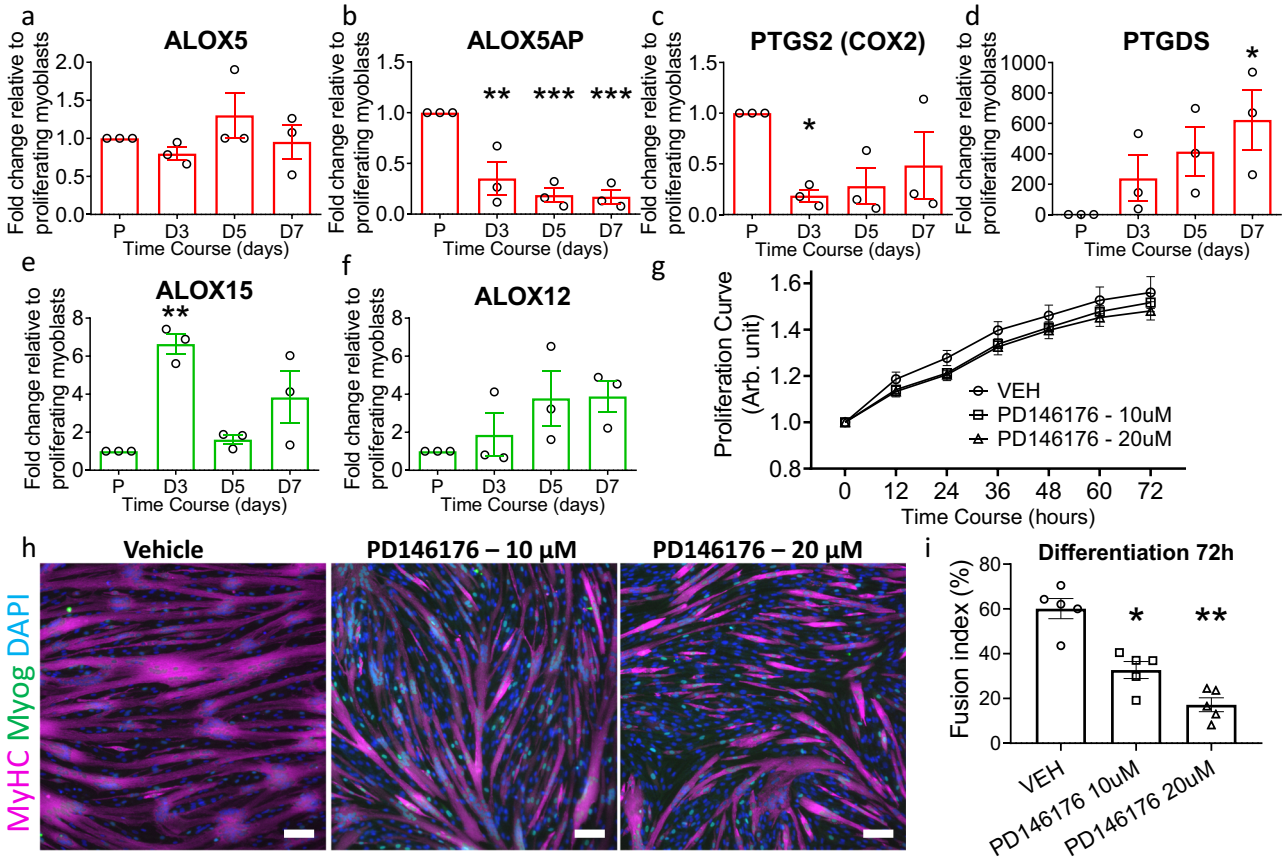


Fig. 5 | ALOX15 pharmacological inhibition impairs human myogenic cells differentiation. a–h Expression quantification by qPCR of the enzymes *ALOX5* (**a**), *ALOX5AP* (**b**) (P vs. D3 $p = 0.0037$; P vs. D5 $p = 0.0009$; P vs. D7 $p = 0.0008$), *PTGS2* (**c**) (P vs. D3 $p = 0.0392$), *PTGDS* (**d**) (P vs. D7 $p = 0.0429$), *ALOX15* (**e**) (P vs. D3 $p = 0.0089$), and *ALOX12* (**f**) in human myogenic cells during in vitro myogenesis. Pro-inflammatory enzymes are identified in red, pro-resolving enzymes are identified in green. **g** Growth curve of human myoblasts treated with the ALOX15 inhibitor PD146176 (10 µM, 20 µM) or vehicle (VEH) for 3 days in proliferation medium. **h** Representative images of human myogenic cells at 3 days of differentiation immunostained for Myosin heavy chain (MyHC, pink), Myog (green), and DAPI (blue). Scale bars = 50 µm. **i** Fusion index of human myoblasts treated with PD146176 (10 µM, 20 µM) or vehicle (VEH) for 3 days in differentiation medium (VEH vs. PD146176 10 uM $p = 0.00141$; VEH vs. PD146176 20 uM $p = 0.0011$). Results are expressed as mean +/- SEM. Biological replicates $n = 3$ for panels **a**–**f**; $n = 5$ for panels **g**, **i**. * $p < 0.05$, ** $p < 0.01$, *** $p < 0.001$. One-way ANOVA with Dunnett's multiple comparisons test (**a**–**f**). Repeated measure 2-way ANOVA with Uncorrected Fisher's LSD multiple comparisons test (**g**). 2-way Paired t-test (**i**). Source data are provided as a Source Data file.

resolution phase. Similar to what was observed at 7 dpi, there is a decrease in the number of Myog+ cells at 14 dpi; however, the number of Pax7+ cells is not significantly changed at that time point (Fig. 6k–m). Moreover, the reduction in the MFD is still observed at 14 dpi in the *Alox15*-KO muscle compared to WT (Fig. 6n, o).

Considering that the *Alox15*-KO model is a whole-body knockout that can affect different cell types, including immune cells, we performed a cell transplantation assay to assess if an intrinsic defect is observed specifically in *Alox15*-KO myoblasts (Fig. 6p). To do so, TA muscle of dystrophin-deficient mdx mice (immunosuppressed with FK-506) were CTX-injured and myoblasts from *Alox15*-KO or WT mice were transplanted in each regenerating TA. Myoblast fusion capacity into newly formed fibers was assessed at 14 dpi by counting the number of dystrophin-positive fibers (Fig. 6q). The quantity of dystrophin-expressing myofibers was significantly lower in the TA transplanted with *Alox15*-KO myoblast compared to WT (Fig. 6r).

Altogether, these findings demonstrate that *Alox15*-mediated bioactive lipid class switching contributes to muscle regeneration in vivo by promoting myogenic cell differentiation and myofiber growth.

Protectin D1 rescues *Alox15*-KO defect during regeneration

Next, the ability of SPMs to rescue the regeneration deficit observed in *Alox15*-KO mice was evaluated. To do so, we focused on PD1, a DHA-derived bioactive lipid with potent pro-resolving and anti-inflammatory capacities[41]. This lipid mediator was chosen because; 1) Its biosynthesis is entirely dependent on Alox15 (while other mediators could also rely partly on Alox5); 2) the level of PDX, its synthesizing enzyme, and its receptor are increased in myogenic cells during differentiation; 3) transcriptomics datasets showed that its receptor Gpr37 is expressed specifically in MuSCs and myotubes but not in fibro-adipogenic progenitors or macrophages (M0, M1, M2) (Supplementary Fig. 6). We investigated the therapeutic capacity of PD1 instead of its positional isomer PDX because it has been shown to have stronger anti-inflammatory capacities in vivo compared to PDX, which was less potent at the same dosage[42].

We first investigated the effect of PD1 in vitro. In WT myoblasts, treatment with PD1 during differentiation increased their fusion capacity (Fig. 7a, b). Next, we investigated the activation of signaling pathways by PD1, by treating myoblasts with PD1 for 0, 15, 30, 60, or 120 min. Western blot analysis revealed that the addition of PD1 to the medium of myoblasts activated the ERK1/2 pathway (Fig. 7c, d).

To evaluate the capacity of PD1 treatment to rescue muscle regeneration in vivo, *Alox15*-KO mice were injured by cardiotoxin injection and were treated daily with PD1 (5 µg/kg/day, i.p.) (Fig. 7e). At 7 dpi, we observed a reduction in the number of Pax7+ cells while Myog+ cells were not significantly affected; however, the size of the myofibers was increased in the PD1-treated group (Fig. 7f–i). Immunostaining for MYH3 (embryonic MyHC) revealed a reduction in the

https://doi.org/10.1038/s41467-025-60586-8

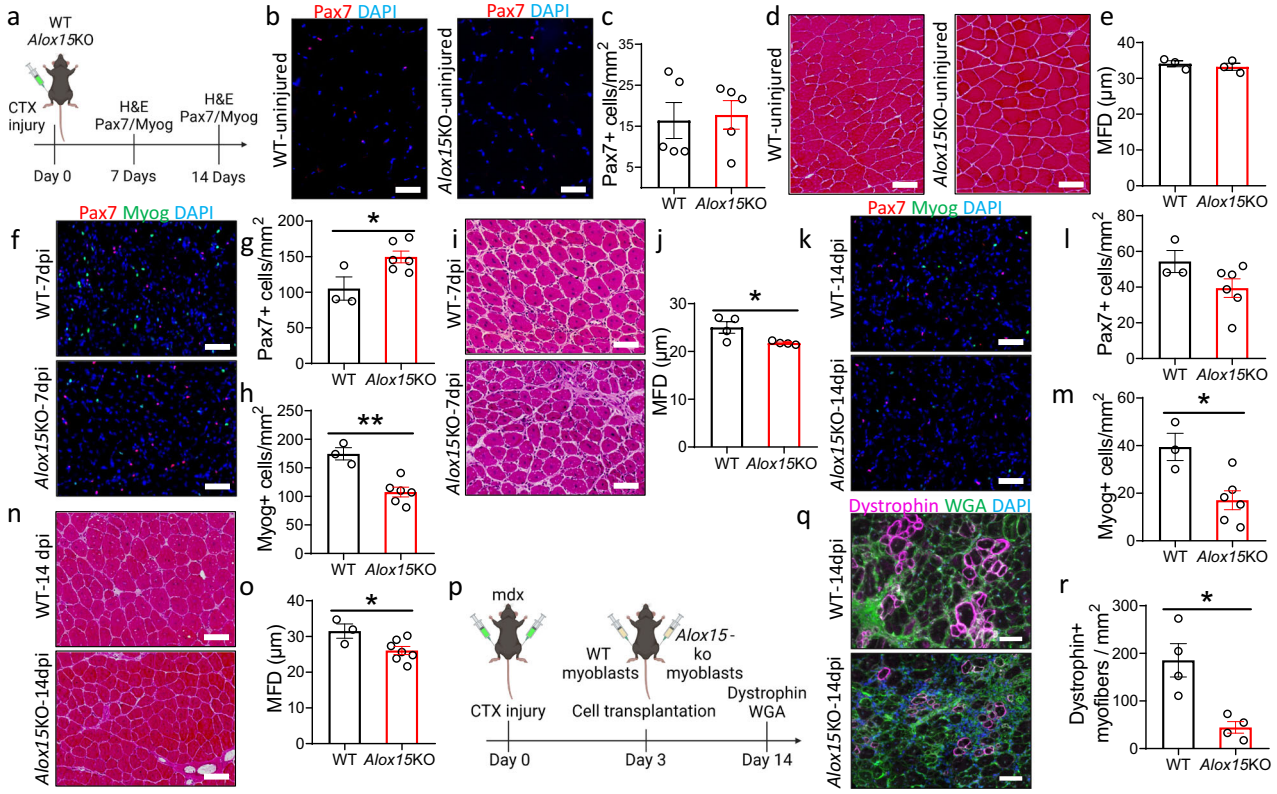


Fig. 6 | Alox15-KO mice display impaired regeneration. a Schematic showing the timeline of cardiotoxin (CTX) injury experiment and muscle collection at 7- and 14-days post injury (dpi) (Created in BioRender)[92]. **b** Representative images of Pax7 (red), DAPI (blue) staining on muscle sections of *tibialis anterior* (TA) muscle of uninjured WT and *Alox15*-KO mice. Scale bars = 50 µm. **c** Quantification of Pax7+ cells in TA muscles of uninjured WT and *Alox15*-KO mice. **d** Representative images of H&E staining on muscle sections of TA muscle of uninjured WT and *Alox15*-KO mice. Scale bars = 50 µm. **e** Quantification of the minimal fiber diameter (MFD) in TA muscles of uninjured WT and *Alox15*-KO mice. **f** Representative images of Pax7 (red), Myog (green), DAPI (blue) staining on muscle sections of TA muscle of WT and *Alox15*-KO mice at 7 dpi. Scale bars = 50 µm. **g, h** Quantification of the number of Pax7+ (**g**) ($p = 0.0287$) and Myog+ (**h**) ($p = 0.0022$) cells in TA muscles of WT and *Alox15*-KO mice at 7 dpi. **i** Representative images of H&E staining on muscle sections of TA muscle of WT and *Alox15*-KO mice at 7 dpi. Scale bars = 50 µm. **j** Quantification of the minimal fiber diameter in TA muscles of WT and *Alox15*-KO mice at 7 dpi ($p = 0.0377$). **k** Representative images of Pax7 (red), Myog (green), DAPI (blue) staining on muscle sections of the TA muscle of WT and *Alox15*-KO mice at 14 dpi. Scale bars = 50 µm. **l, m** Quantification of the number of Pax7+ (**l**) and Myog+ (**m**) ($p = 0.0143$) cells in the TA muscles of WT and *Alox15*-KO mice at 14 dpi. **n** Representative images of H&E staining on muscle sections of the TA muscles of WT and *Alox15*-KO mice at 14 dpi. Scale bars = 50 µm. **o** Quantification of the minimal fiber diameter in the TA muscles of WT and *Alox15*-KO mice at 14 dpi ($p = 0.0355$). **p** Schematic showing the timeline of mdx mice CTX-injury experiment followed by the transplantation of WT and *Alox15*-KO myoblasts in the right and left TA muscles at 3 DPI and muscle collection at 14 dpi (Created in BioRender)[92]. **q** Representative images of Dystrophin (pink), WGA (green), DAPI (blue) staining on muscle sections of TA muscle of mdx mice at 14 dpi. Scale bars = 75 µm. **r** Quantification of Dystrophin+ myofibers in TA muscles of mdx mice at 14 dpi transplanted with WT or *Alox15*-KO myoblasts ($p = 0.0336$). Results are expressed as mean +/- SEM. Black bars represent the WT group and red bars are the *Alox15*-KO group. Biological replicates $n = 5$ for panel (**c**); $n = 3$ for panel (**e**); $n = 3$ for WT and $n = 6$ for *Alox15*KO for panels (**g, h, l, m**); $n = 4$ for panels (**j, r**); $n = 3$ for WT and $n = 7$ for *Alox15*KO for panel (**o**). * $p < 0.05$, ** $p < 0.01$, *** $p < 0.001$. 2-way Unpaired t-test. Source data are provided as a Source Data file.

number of newly formed regenerating myofibers (Fig. 7j, k). To determine if this reduction was caused by an accelerated regeneration process, we performed a staining for dystrophin, which is only expressed in mature regenerated myofibers[43]. We observed that PD1 treatment increased the number of dystrophin-positive mature myofibers (Fig. 7l, m). At 14 dpi, immunostaining of muscle sections showed that PD1 treatment does not affect the number of myogenic cells (Pax7+ or Myog+) but increases the size of the regenerating myofibers (Fig. 7n–q). Altogether, these results suggest that PD1 treatment holds therapeutic potential to enhance muscle regeneration following injury.

PD1 ameliorates muscle phenotype in dystrophic mdx mice

Considering the benefits of PD1 on muscle regeneration, we evaluated its therapeutic potential for the treatment of muscular diseases. Particularly, we focused on assessing the effect on DMD because: 1) DMD muscles are subjected to ongoing cycles of degeneration and regeneration, and 2) the myogenic cells showed a reduced regenerative capacity in different DMD models[44–49]. We used the mdx mouse, a well-characterized and widely used model that carries a mutation in the *Dmd* gene, leading to a lack of dystrophin similar to what is observed in DMD patients, although the phenotype is milder than that observed in humans. Daily injections of PD1 (5 µg/kg/day, i.p.) or vehicle were administered to mdx mice for 21 days (Fig. 8a). Immunostaining for Pax7 and Myog showed a modest increase of 15% in the number of Pax7+ cells, and a stronger increase of >2.3 fold in the number of Myog + cells (Fig. 8b–d). Analysis of muscle fiber size showed that PD1-treated mdx mice have higher cross-sectional area (CSA) in comparison to the vehicle-treated mice (Fig. 8e, f). Moreover, an assessment of the number of nuclei per myofiber revealed that PD1-treated mdx mice display a higher number of myonuclei per fiber compared to the vehicle-treated mice (Fig. 8g). Analysis of ex vivo muscle function of the EDL muscle isolated from mdx mice showed that PD1-treated mice have greater maximal force compared to vehicle-treated mdx mice (Fig. 8h, and Supplementary Fig. 7). Altogether, these results provide proof-of-concept that Alox15-derived pro-resolving lipids such as PD1 can enhance muscle regeneration and alleviate disease progression in a model of DMD.

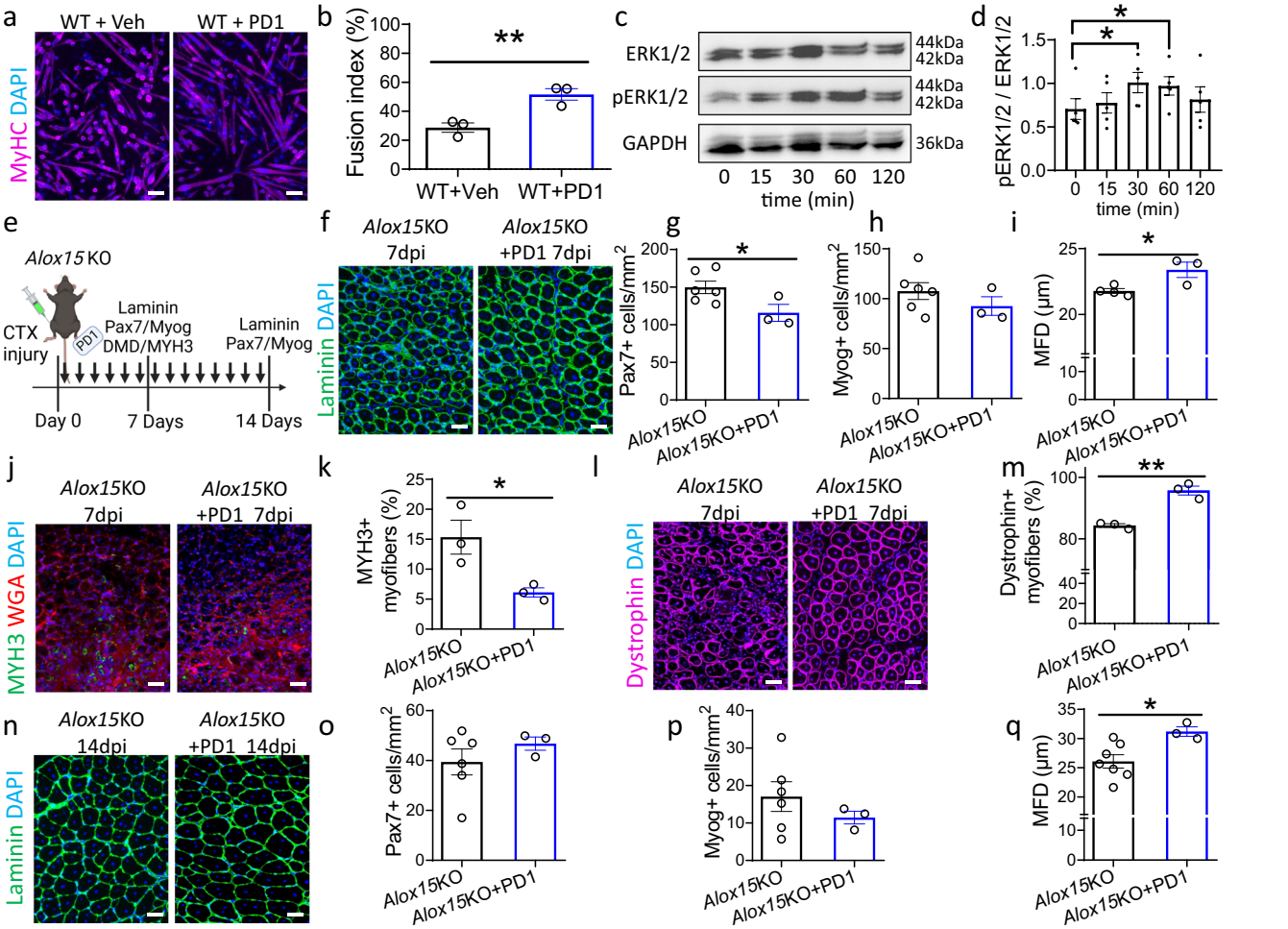


Fig. 7 | Protectin D1 enhances muscle regeneration. a Representative micrographs showing myosin heavy chain (MyHC, fuchsia) and DAPI (nuclei, blue) staining on myoblasts differentiated for 2 days and treated (twice per day) with Vehicle (Veh) or protectin-D1 (PD1). Scale bars = 50 µm. **b** Quantification of the fusion index of WT myoblasts differentiated for 2 days and treated with Vehicle (Veh) or protectin-D1 (PD1) ($p = 0.0017$). **c, d** Representative Western blots and quantification of ERK1/2 phosphorylation in myoblasts treated with PD1 for 0, 15, 30, 60, 120 min (0 vs. 30 $p = 0.0282$; 0 vs. 60 $p = 0.0191$). **e** Schematic showing the timeline of daily intraperitoneal (i.p.) injection of Protectin-D1 (PD1, 5 ug/kg/day), or vehicle (Veh) in *Alox15*-KO mice after cardiotoxin (CTX) injury (Created in BioRender)[93]. **f** Representative images of Laminin (green), DAPI (blue) staining on muscle sections of *tibialis anterior* (TA) muscle of *Alox15*-KO mice at 7 dpi (dpi) and injected daily with PD1 or Veh. Scale bars = 50 µm. **g–i** Quantification of Pax7+ cells (**g**) ($p = 0.0494$), Myog+ cells (**h**), and the minimal fiber diameter (MFD) (**i**) ($p = 0.0301$) in the TA muscles of *Alox15*-KO mice at 7 dpi (dpi) and injected daily with PD1 or Veh. **j** Representative images of embryonic MyHC (MYH3, green), Wheat Germ Agglutinin (WGA; connective tissue marker; red), DAPI (nuclei, blue) staining on sections of the TA muscle of *Alox15*-KO mice at 7 dpi and injected daily with PD1 or Veh. Scale bars = 50 µm. **k** Quantification of the number of MYH3+ myofibers in the TA muscles of *Alox15*-KO mice at 7 dpi and injected daily with PD1 or Veh ($p = 0.0348$). **l** Representative images of Dystrophin (fuchsia) and DAPI (nuclei, blue) staining on sections of the TA muscle of *Alox15*-KO mice at 7 dpi and injected daily with PD1 or Veh. Scale bars = 50 µm. **m** Quantification of the number of Dystrophin+ myofibers in the TA muscles of *Alox15*-KO mice at 7 dpi and injected daily with PD1 or Veh ($p = 0.0018$). **n** Representative images of Laminin (green) and DAPI (blue) staining on muscle sections of the TA muscle of *Alox15*-KO mice at 14 dpi and injected daily with PD1 or Veh. Scale bars = 50 µm. **o–q** Quantification of Pax7+ cells (**o**), Myog+ cells (**p**), and the minimal fiber diameter (**q**) ($p = 0.025$) in the TA muscles of *Alox15*-KO mice at 14 dpi and injected daily with PD1 or Veh. Results are expressed as mean +/- SEM. Black bars represent the *Alox15*-KO group and blue bars are *Alox15*-KO + PD1 group. $n = 3$ for panels (**b, k, m**); $n = 5$ panel (**d**); $n = 6$ for *Alox15*KO and $n = 3$ for *Alox15*KO + PD1 for panels (**g, h, o, p**); $n = 4$ for *Alox15*KO and $n = 3$ for *Alox15*KO + PD1 for panel (**i**); $n = 7$ for *Alox15*KO and $n = 3$ for *Alox15*KO + PD1 for panel (**q**). $^*p < 0.05$, $^{**}p < 0.01$, $^{***}p < 0.001$. 2-way Paired t-test (**b**), One-way repeated measure ANOVA with Uncorrected Fisher's LSD multiple comparisons (**d**), 2-way unpaired t-test (**g–i, k, m, o–q**). Source data are provided as a Source Data file.

Discussion

Our findings show that myogenic cells actively secrete bioactive lipids from eicosanoid and docosanoid classes, express their biosynthetic enzymes, and receptors. This bioactive lipid profile in mouse and human myogenic cells evolves during myogenesis progression from a pro-inflammatory to a pro-resolving signature. Furthermore, we showed that specific lipid mediators can also directly target myogenic cells to regulate their cell fate decision. Further, using *Alox12/15*-knockout and inhibitors, we demonstrated that blocking the bioactive lipid class switching results in impaired myogenic progression. Finally, we discovered that the pro-resolving lipid mediator PD1 could be used as a therapeutic avenue to accelerate muscle regeneration after injury and ameliorate the muscle phenotype in DMD. Overall, our findings provide insights on a novel regulatory mechanism controlling myogenic progression.

Bioactive lipid class switching has been well-characterized during the inflammatory process to regulate macrophages transition from pro-inflammatory to pro-resolving phenotype. The stimulation of M1 macrophage polarization (IFNγ) was shown to induce an increase in *Alox5* expression, while the M2 macrophage polarization (IL-4) induces

https://doi.org/10.1038/s41467-025-60586-8

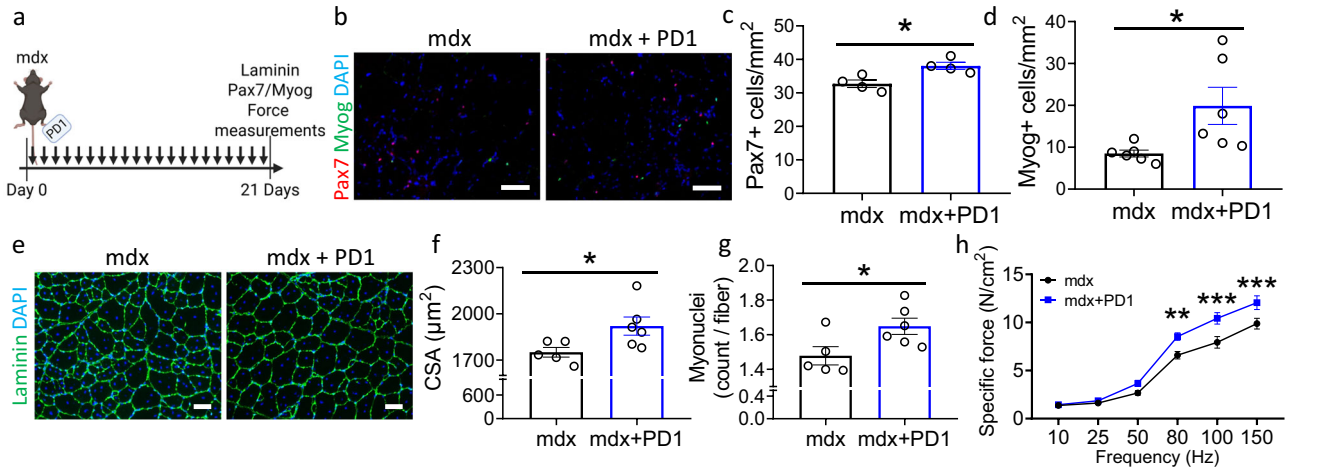


Fig. 8 | Protectin D1 promotes muscle regeneration in mdx mice. a Schematic showing the timeline of daily intraperitoneal (*i.p.*) injection of Protectin-D1 (PD1, 5 ug/kg/day), or vehicle (Veh) in *mdx* mice for 21 days (Created in BioRender)[94]. **b** Representative micrographs of Pax7 (red), Myog (green), and DAPI (nuclei, blue) staining on sections of the tibialis anterior (TA) muscles of mdx mice treated with PD1 or vehicle. Scale bars = 50 µm. **c, d** Quantification of the number of Pax7+ (**c**) ($p = 0.0137$), and Myog+ (**d**) ($p = 0.0303$) cells in muscles of mdx mice after 21 days of PD1 or Veh treatment. **e** Representative micrographs of Laminin (green), DAPI (nuclei, blue) staining on muscle sections of the TA muscle of mdx mice after 21 days of PD1 or Veh treatment. Scale bars = 50 µm. **f, g** Quantification of the cross-sectional area (**f**) ($p = 0.0414$) and number of myonuclei per fiber (**g**) ($p = 0.0376$) in the TA muscles of mdx mice after 21 days of PD1 or Veh treatment. **h** Isometric contractile properties of EDL muscles showing the specific force of *mdx* mice treated daily for 21 days with PD1 or Veh (80hz $p < 0.0017$; 100hz; $p < 0.0001$; 150hz; $p = 0.0005$). Results are expressed as mean +/- SEM. Black bars represent the *mdx* group and blue bars are *mdx* + PD1 group. Biological replicates $n = 4$ for panel c, $n = 6$ for panel d; $n = 5$ for *mdx* and $n = 6$ for *mdx* + PD1 for panels (**f, g**); $n = 5$ for panel (**h**). $^{*}p < 0.05$, $^{**}p < 0.01$, $^{***}p < 0.001$. 2-way Unpaired t-test (**c, d, f, g**), 2-way ANOVA with Uncorrected Fisher's LSD multiple comparisons test (**h**). Source data are provided as a Source Data file.

an increase in Alox15 expression and the downstream pro-resolving lipids[50]. During muscle regeneration, the transition from Ly6C^{hi} to Ly6C^{lo} macrophages between 2 and 4 dpi is associated with a switch in bioactive lipid from pro-inflammatory (e.g., PGE_2) to pro-resolving lipids (e.g., RvD2, LXA_4)[27]. The treatment of macrophages with the pro-resolving lipid RvD2 was shown to trigger the macrophage switch toward their pro-resolving phenotype in vitro and in vivo[31]. Moreover, RvD2-treated macrophages produce pro-myogenic paracrine factors that stimulate myoblast differentiation and fusion in vitro[31].

Our findings support that bioactive lipid class switching is a conserved mechanism that plays a significant role in guiding myogenic cell fate decisions during myogenesis progression. Although the drastic switch in bioactive lipid expression observed in vitro may be amplified due to the abrupt change in culture medium, a similar bioactive lipid profile change is also evident in vivo, supporting its physiological relevance. Noteworthy, the change in bioactive lipid expression from myoblast proliferation to differentiation occurs during the same period as the macrophage phenotype switch during muscle regeneration[35], suggesting that these two biological processes could be interrelated. Therefore, the release of bioactive lipids in the myogenic cells' microenvironment could also have paracrine effects that coordinate the activity of the different cell types during muscle regeneration. Supporting this hypothesis, it was shown that the treatment of myoblasts in vitro with the pro-resolving lipid RvD1 induced an immunomodulatory effect that reduces their expression of pro-inflammatory cytokines (e.g., IL-6, TNF-α, MCP-1)[30].

In addition to their role during inflammation, bioactive lipids were also shown to play a role in stem cell biology[51]. Different stem cell types, such as human periodontal ligament stem cells[52], mesenchymal stem cells[53], and embryonic stem cells[54], were shown to produce bioactive lipids. Moreover, bioactive lipids can also directly target specific GPCRs on stem cells to affect their function and cell fate decision[51]. For instance, lipoxin-A4 was shown to target the FPR2 receptor on periodontal ligament stem cells to enhance their migration, proliferation, and regenerative capacity[52]. The pro-resolving bioactive lipid Protectin D1 was shown to promote the neuronal differentiation of embryonic stem cells[55]. Our findings add to this emerging literature by showing that bioactive lipid class switching plays a role in the regulation of myogenic cell fate decisions during myogenic progression.

Our results indicate that the pro-inflammatory enzyme COX-2 and its downstream lipid mediators (e.g., prostaglandins) are predominantly expressed in proliferating myoblasts. These findings are consistent with previous studies that demonstrated that PGE_2 plays a crucial role for MuSC proliferation and symmetric division[28,29]. We showed that PGE_2 administration stimulates the expression of the pro-inflammatory enzyme COX-2, upregulates the *Ep4* receptor, and downregulates the prostaglandin degradation enzyme *Hpgd*, which supports that this molecule plays a positive feedback loop that further stimulates PGE_2 signaling activity and consequently myogenic cell proliferation. These findings contrast with the ones observed in polymorphonuclear cells, in which PGE_2 stimulates the bioactive lipid class switch by increasing the production of Alox12 and Alox15[11,56]. This difference could be mediated by the different receptors expressed by polymorphonuclear cells (predominantly EP2 and EP4) compared to myogenic cells (EP4 only)[29,57]. Treatment with PGE_2 in myogenic cells also increased the enzymes Alox5 and Alox5AP, which are predominantly expressed in proliferating myoblasts compared to differentiated myoblasts/myotubes. While these enzymes can participate in the formation of pro-resolving molecules, such as lipoxins, it was shown using *Alox5*-knockout models that their effect is primarily pro-inflammatory[58,59]. We have identified that contrarily to other COX2-derived pro-inflammatory enzymes Lipocalin-Type Prostaglandin D Synthase (L-PGDS, the enzyme encoded by *Ptgds*) increases during differentiation, together with the rise in PGD_2 levels. We have demonstrated that the PGD_2-derivative 15Δ-PGJ_2 participates to the bioactive lipid class switch by increasing the expression of the prostaglandin-degrading enzyme *Hpgd*, thereby triggering a negative feedback loop reducing the pro-inflammatory/pro-resolving lipid ratio. PGD_2 and 15Δ-PGJ_2 were shown to reduce the production of inflammatory cytokines in antigen-presenting cells by acting through different pathways such as the activation of Nrf2 and PPARγ pathways, and the inhibition of NF-kB pathway[60–63]. Moreover, the pro-resolving

role of L-PGDS has been described in autoimmune diseases such as osteoarthritis[64].

We observed that *Alox15*-KO is not impacting the biosynthesis of pro-inflammatory lipid mediators such as PGE_2, $PGF_{2\alpha}$, and TXB_2, which was expected considering that these bioactive lipids rely on COX-2 expression. However, we unexpectedly observed that *Alox15*-KO blocks the rise in PGD_2 expression during differentiation. These results suggest that there is retroactive feedback by which Alox15-derived pro-resolving lipids stimulate PGD_2 expression. Supporting this observation, a study using lung fibroblasts showed that LPS induces biphasic expression of prostaglandins. The authors showed that resolvin-D1 decreases the initial peak of PGE_2 at 6 h but enhances the second peak of PGD_2 at 48h[65]. Overall, the bioactive lipid class switch requires a complex interplay between pro-inflammatory and pro-resolving lipids.

Our findings show that the expression of many bioactive lipid receptors follows a similar pattern to the expression of their ligands during myogenic progression. For instance, the decrease in PGE_2 and PGF_2 is associated with a decrease in their respective receptors *Ep4* and *Fp* (Prostaglandin F receptor) during myogenesis. Similarly, the increase in PGD_2 and PDX is coupled with an increase in their receptors *Dp2* and *Gpr37*. However, some ligand-receptor pairs such as TXB_2/*Tp* or LXA_4/*Fpr2* were inversely related. These results suggest that there is a complex crosstalk by which bioactive lipids could signal to myogenic cells at different stages of myogenesis. For instance, the pro-resolving lipid $RvD5_{n\text{-}3DPA}$ produced predominantly by differentiated myotubes could act on proliferative myoblasts that express higher levels of the receptor *Gpr101*. Similar inter-myogenic stage communication was observed for proteins such as Wnt7a that is produced by regenerating myofibers and binds to the Fzd7 receptor expressed by MuSCs to induce their symmetric division[66].

Our in vitro findings show that impairment in the bioactive lipid class switching in *Alox15*-KO myoblasts does not affect cell proliferation but impairs cell differentiation. Similar findings were observed using different ALOX15 inhibitors in human myogenic cells. In vivo experiments showed that muscle injury in *Alox15*-KO mice does not reduce Pax7+ MuSCs/proliferative myoblasts but decreases Myog+ differentiated myoblasts and the size of the newly formed fibers. Moreover, the myoblast transplantation experiment allowed us to demonstrate the impaired fusion capacity of *Alox15*-KO myoblasts independently of their microenvironment. These findings suggest that the lack of Alox15 in myogenic cells intrinsically affects their myogenesis capacity, but it does not exclude that the microenvironment is also defective in *Alox15*-KO mice. Consistent with this, a very recent study observed an imbalanced immune response and intrinsic defects in myogenic cell fate determination leading to impaired regeneration post-injury in *Alox15*-KO models[67].

Our findings suggest that the role of Alox15-derived bioactive lipids is time-dependent, as Alox15 deficiency does not impact myogenic cell proliferation during the early stages of regeneration but regulates myogenic cell differentiation at later stages. Moreover, it is also context-dependent, as the lack of Alox15 does not influence MuSC pool or myofiber size in uninjured muscle. Supporting this observation, it was previously shown that Alox15 expression increases following muscle denervation, and its genetic or pharmacological ablation reduces denervation-induced muscle atrophy, which suggests that Alox15-derived bioactive lipids could play a negative role when chronically upregulated[68]. Altogether, these findings suggest that Alox15-derived bioactive lipid expression needs to be tightly regulated and precisely coordinated.

Our findings suggest that PD1 regulates the late myogenic stages, which is coherent with the continuous increase in the expression of its receptor Gpr37 during the time course of myoblast differentiation/fusion. PD1 could mediate its effect, in part, by activating the ERK1/2, which can have pro- or anti-differentiation effects depending on the context. In C2C12 myoblasts, it was shown that ERK2 is required for differentiation, while ERK1 was dispensable[69]. It was also demonstrated that stimulating ERK1/2 signaling can restore myogenic differentiation in a model of hypoxia[70]. Previous findings also showed that PDX can target C2C12 myotubes to activate AMPK signaling and the expression of myokine (IL-6), which could stimulate insulin sensitivity in obese diabetic mice[71]. Another study demonstrated that the expression of pro-resolving lipids, including PD1 and PDX is deficient in the muscles of aged mice, which was associated with excessive inflammation, poor myofiber regeneration, and delayed functional recovery[72]. PD1 is investigated as a therapeutic avenue for mitigating different immune-related conditions such as acute kidney injury[73], psoriasis[74], and asthma[75]. We now demonstrate that PD1 could be used as a therapeutic avenue in a model of DMD by acting on the late myogenic stages, increasing myofiber size and muscle strength. These results are coherent with our previous findings showing that treatment of myoblasts with the pro-resolving lipid RvD2 does not affect myoblast proliferation, but stimulates myoblast differentiation by targeting the Gpr18 receptor[31,76]. Similarly, in another study, where they performed a drug screen on bioactive lipids, the authors identified that lysophosphatidic acid and niflumic acid can stimulate myogenic cell engraftment by stimulating fusogenic genes (e.g. myomaker) without impacting on their proliferative ability[77]. Considering that our findings show that the level of pro-resolving receptors varies greatly during myogenesis progression, it is expected that different types of bioactive lipids could target the different stages of myogenesis.

Overall, our findings demonstrate that the bioactive lipid class switching process is a conserved regulatory mechanism during myogenesis. Impairment in this process results in delayed myogenic cell progression. These results have potential implications for therapeutic intervention in muscle regeneration and diseases. Particularly, these molecules hold therapeutic potential for the treatment of recently described satellite cell-opathies that affect the myogenic capacity of MuSCs[78,79]. A better understanding of the underlying mechanisms regulating myogenesis opens the opportunity to intervene and modulate myogenic cell function at specific steps of myogenesis to improve muscle regeneration and function.

Methods

Human samples and ethics approval

Human myogenic cells were obtained from a previous study in which muscle biopsies were collected from the vastus lateralis of healthy individuals (4 men and 1 woman, average age: 42.8 + /− 19.3 years old) using the modified Bergstrom needle technique with suction[80]. Participants received a compensation for their involvement in the study. Cells were grown in Sk-MAX media complemented with Sk-MAX supplement and 20% fetal bovine serum (FBS). Myoblasts were purified by positive magnetic immunoselection using CD56 MicroBeads according to the manufacturer's instructions (Miltenyi Biotec). Myoblast differentiation was induced by low-serum medium (2% horse serum (HS) in DMEM). Myoblasts were treated with vehicle (DMSO) or ALOX15 inhibitor PD146176 at 10 μM[36] and 20 μM[37] and Baicalein at 10 μM[40] and 20 μM[81] every day for 3 days. This study was approved by the Ethics review board of the Centre intégré universitaire de santé et de services sociaux du Saguenay−Lac-Saint-Jean, Canada (#2019-036), in accordance with the principles of the declaration of Helsinki. Written informed consent has been obtained from participants. No sex or gender analysis was carried out on human samples considering the small number of samples available.

Animals and experimental design

Eight to twelve-week-old male mice (Mus Musculus) C57BL/6 J (WT), B6.129S2-Alox15tm1Fun/J (Alox15-KO) and mdx mice (Strain #000664, #002778, #001801 Jackson Laboratory; Bar Harbor, ME) were housed within the Animal Holding Facility at the CHU Sainte-Justine (Montreal,

CA) on a 12:12 h light:dark cycle at 21 °C and 40% humidity in pathogen-free cages with free access to food and tap water. We considered biological sex in our study design by using only male mice, since DMD is an X-linked disorder that almost exclusively affects males. In every experiment, age-matched mice served as control. WT and *Alox15*-KO mice were injured by cardiotoxin (CTX, 10 µM; Latoxan, cat. no. L8102) injection in the right TA muscle. *Alox15*-KO mice were randomly assigned to two experimental groups that received daily intraperitoneal (i.p.) injections of saline (control) or PD1 (5 µg/kg/day). After 7 or 14 days of treatment, TA muscle function was recorded, and muscles were collected, weighed, and embedded in freezing medium (Tissue-Tek O.C.T.) before being rapidly frozen in liquid nitrogen-cooled isopentane and stored at − 80 °C prior to sectioning and staining. Mice were euthanized by CO_2 inhalation (under anesthesia) followed by cervical dislocation. All animal experiments were approved by the CHU Sainte-Justine Research Ethics Committee and performed in compliance with the *Comité Institutionnel des Bonnes Pratiques Animales en Recherche* (CIBPAR; approval number 2022-3608) in accordance with the Canadian Council on Animal Care guidelines.

Ex vivo muscle contractility

To assess muscle force, the EDL muscle was carefully isolated and placed in a buffered physiological solution (Krebs-Ringer supplemented with glucose and bubbling carbogen gas) maintained at 25 °C. The muscles were attached by the tendons to an electrode at one end and to a lever arm at the other end. Optimal muscle length (L_0) was determined and gradually adjusted until the maximum isometric twitch tension was achieved. The EDL is given a 10 min equilibration in the bath prior to the measurement of contractile properties. A force-frequency curve was established by stimulating the muscles at different frequencies, ranging from 10–150 Hz, with a 2 min rest between each stimulation (ASI 611 A Dynamic Muscle Analysis v5.300). Thereafter, muscle length and weight were measured to assess specific muscle force (N/cm^2). To do so, a mathematical approximation of the cross-sectional area was calculated based on the formula: Specific force (N/cm^2) = (absolute force (N) × fiber length ($0.44 \times L_0$ for the EDL muscle) × muscle density (1.06 g/cm^3))/muscle mass (g).

MuSC isolation and primary myoblast culture

Muscles from both hindlimbs of mice were collected, minced with scissors, and dissociated in collagenase (Roche) / dispase (Sigma) using the gentle MACS dissociator (Miltenyi Biotech). The homogenate was filtered through a 100 µm and a 30 µm cell strainer, and stained with the following antibodies for 20 min on ice in the dark: anti-CD45 FITC-conjugated (clone 30F11; 1:10; Miltenyi Biotech # 130-116-535), anti-CD31 FITC-conjugated (Clone 390; 1:10; Miltenyi Biotech #130-123-675), anti-CD11b FITC-conjugated (M1/70.15.11.5; 1:10; Miltenyi Biotech #130-113-234), anti-Sca-1 BV421-conjugated (D7; 1:25; Biolegend #108128), anti-Itgb1 APC-conjugated (clone HMβ1-1; 1:3; Miltenyi Biotech #130-102-557), and anti-Itga7 PE-conjugated (clone 3C12, 1:15; Miltenyi Biotech #130-120-812), and 7-AAD (1:6; Biolegend #420404). MuSCs were isolated by FACS using a gating strategy based on forward scatter and side scatter profiles, cell viability (7AAD), negative selection with FITC-and BV421 conjugated antibodies, and positive selection for APC and PE (Supplementary Fig. 1).

Isolated cells were cultured in collagen-coated Petri dishes with proliferation medium (Ham's F10 media (GIBCO) containing 20% FBS (Wisent), 1% penicillin–streptomycin (GIBCO), and 2.5 ng/mL bFGF (Wisent)). Cells were treated daily with PGE_2 (250 nM), PGD_2 (250 nM), 15Δ-PGJ_2 (250 nM), PD1 (250 nM), or vehicle for 24 h, 48 h, 72 h, 96 h or 120 h to assess myoblast proliferation, differentiation, and fusion. To assess proliferation, the cells were incubated in the IncuCyte (Essen Bioscience; Incucyte 2022B Rev2), an automated microscope located in the cell culture incubator that automatically takes pictures and performs unbiased analysis of cell number and density. To assess differentiation, the cells were incubated in a low-serum differentiation medium (48.5% Ham's F10, 48.5% DMEM low glucose, 1% penicillin–streptomycin, 2% HS).

Transplantation

Myoblast transplantation was performed on mdx mice immunosuppressed by the subcutaneous implantation of an osmotic pump (Alzet, Model 2004) containing FK506 (20 mg/ml; tacrolimus, Lc Laboratories, F-4900). Mice were injured with CTX 3 days prior to the cell transplantation as previously described[79]. A total of 1×10^6 myoblasts were diluted in 20 µl of saline (0.9% NaCl sterile solution) and injected in the injured TA muscle[82]. Each mouse was injected with WT myoblasts and *Alox15*-KO myoblasts, in their right and left TA muscles, respectively. Muscles were collected at 14 dpi and myoblast fusion capacity was assessed by dystrophin immunostaining.

Immunofluorescence and histology

Immunofluorescence staining was performed on cultured cells or on muscle sections[83]. Sections of 10 µm thickness were cut with a cryostat (NX50, Thermo Fisher) from the proximal and distal half of the TA muscle, mounted on Superfrost Plus slides (Thermo Fisher Scientific, Canada), and fixed with 4% PFA for 10 min. Cultured cells were fixed with 2% PFA for 10 min. After being washed, the samples were permeabilized with 0.2% Triton X-100, 0.1 M Glycine for 10 min. Samples were blocked with mouse-on-mouse blocking reagent (Vector labs), 5% goat serum (Wisent), and 2% BSA in PBS for 60 min at room temperature. Samples were incubated overnight at 4 °C with the following primary antibodies: mouse anti-Pax7 (clone PAX7, 1:3; Developmental Studies Hybridoma Bank (DSHB), created by the NICHD of the NIH and maintained at The University of Iowa), mouse anti-MyoD1 (cat# 377460; clone G-1; 1:250; Santa Cruz Biotechnology), rabbit anti-myogenin (#ab124800; clone EPR4789; 1:500; Abcam), mouse anti-Myh3 (clone F1.652; 0.3 µg/ml; DSHB), rabbit anti-Laminin (cat# ab11575; 1:1000; Abcam), rabbit anti-dystrophin (cat# ab15277; 1:1000; Abcam). Samples were washed with PBS and incubated with appropriate cross-adsorbed secondary antibodies (Invitrogen, Thermo Fisher), consisting of either goat anti-rabbit IgG H + L (Alexa Fluor 488, 1:1000), goat anti-mouse IgG1 (Alexa Fluor 546, 1:1000), or goat anti-mouse IgG H + L (Alexa Fluor 488, 1:1000) for 1 h at room temperature. Samples were washed with PBS and counterstained with DAPI. Sections were then mounted with PermaFluor (Thermo Fisher Scientific). Images were viewed and captured on the entire sections using an epifluorescence Leica DM5000 B (Leica Microsystems, Canada; LASX) or EVOS M5000 (Thermo Fisher Scientific; EVOS M5000 Software Revision 1.5.1500.493). Images were then analyzed blindly using the ImageJ Analysis Software Program (version 1.53, National Institutes of Health, Maryland, USA). Myofiber size was analyzed using the MuscleAnalyzer pipeline[84] of the CellProfiler Software (Broad Institute, MIT & Harvard, Cambridge, Massachusetts), and a minimum of 5000 myofibers was calculated per sample. Centronucleation was analyzed using the MyoSight macro of the ImageJ Analysis Software Program[85].

Hematoxylin and Eosin (H&E) staining was performed for the histological characterization of muscles according to standard operating procedures described by TREAT-NMD (MDC1A_M.1.2.004). Sections of 10 µm thickness were fixed with paraformaldehyde (4% PFA) for 10 min, washed for 1 min, incubated with Mayer's hematoxylin solution for 5 min, followed by a 10 min wash in a glass chamber under lukewarm running tap water. Slides were then incubated for 5 min with acetic acid 1% Eosin solution (Merck 1.09844.1000), washed 3 times for 1 min with bidistilled water. Next, the slides were dehydrated by consecutive dipping in 70% ethanol for 1 min, 90% ethanol for 1 min, 100% ethanol for 30 sec and xylene for 30 sec. Coverslips were mounted onto slides using the Eukitt quick-hardening mounting medium

(Sigma-Aldrich, Oakville, Ontario, Canada). The entire sections were captured at 200x magnification using the digital microscope slide scanner (Zeiss AxioScan.Z1).

Western blot

Myogenic cells were lysed with ice-cold RIPA buffer containing 1% of protease inhibitors and centrifuged at 10.000 x g for 10 min. The supernatant was retained, aliquoted, and the protein content was quantified using the BCA Assay Kit (Thermo scientific, Mississauga, Ontario, Canada). Forty micrograms of protein were diluted in a sample buffer (125 mM Tris buffer (pH6.8), 4% SDS, 20% glycerol, 0.05% bromophenol blue, and 200 mM dithiothreitol), heated at 100 °C for 5 min and electro-separated on 8 or 10% sodium dodecyl sulfate-polyacrylamide (SDS) gel. Proteins were transferred to polyvinylidene difluoride membranes, which were blocked with 5% non-fat milk or 5% BSA for 90 min at room temperature, and immunoblotted overnight at 4 °C with either rabbit anti-Alox5 (cat# 3289; clone C49G1; 1:1000 in 5% non-fat milk; Cell signalling technology), rabbit anti-COX2 (cat# ab52237; 1:1000 in 5% non-fat milk; abcam), rabbit anti-Alox15 (cat# LS-C343940-100; 1:1000 in 5% non-fat milk; LSBio), rabbit anti-p44/42 MAPK (ERK1/2, cat#4695; clone 137F5; 1;1000 in 5% BSA: Cell signaling), rabbit anti-p-p44/42 MAPK(T202/Y204) (p-ERK1/2, cat#4370; 9101S; 1;1000 in 5% BSA; Cell Signaling), rabbit anti-β-actin (cat# 4967; 1:1000 in 5% non-fat milk; Cell Signaling Technology), or rabbit anti-GAPDH (cat# 2118; clone 14C10; 1:1000 in 5% non-fat milk; Cell Signaling Technology) as primary antibodies. After washing, membranes were incubated with goat anti-rabbit (H + L) or goat anti-mouse (H + L) HRP-conjugated secondary antibodies (1:3,000; Abcam) for 1 h at room temperature. Bands were revealed with ECL-plus Western blotting reagent (PerkinElmer Life and Analytical Sciences, USA), visualized with the GeneSys image software (Syngene), and quantified using ImageJ (National Institutes of Health, Maryland, USA). After appropriate washing, membrane stripping was performed using 1x Western Blot Stripping Buffer (S208070, ZmTech Scientifique) for 30 mins at room temperature. Then, the membranes were submitted to the same procedure as previously described above. Full blots are presented in the source data file.

qPCR

Total RNA was extracted from myogenic cells using the RNeasy Mini kit (Qiagen, # 74104) according to the manufacturer's instructions. Total RNA was quantified using a Thermo Scientific™ NanoDrop™ 8000 Spectrophotometer. The reverse transcription was conducted with 2 µg of total RNA using the 5X All-In-One RT MasterMix (Abcam, G486 or G592) to obtain cDNA. qPCR was realized with a set of primers designed on Primer-BLAST (NCBI). Gene amplification was realized with the BrightGreen 2X qPCR (Abcam, Mastermix-s-xl) on a Roche LightCycler® 480 Instrument II (LightCycler 480 S 1.5.1). Data were analyzed with the LightCycler® 480 and were normalized relative to *Gapdh* expression for mouse samples and *Rlpo* for human samples. The primers used are shown in Supplementary Table 1.

Targeted lipidomics of bioactive lipids (HPLC-MS/MS)

LXA_4, 15(*R*)-LXA_4, PDX, $RvD5_{n\text{-}3DPA}$, RvE1, PGD_2, PGE_2, $PGF_{2\alpha}$, and TXB_2 were purchased from Cayman Chemical (Ann Arbor, MI, USA). Butylated hydroxytoluene (BHT; cat #W218405) and indomethacin (cat # i7378) was acquired from Sigma-Aldrich (Oakville, ON, Canada). Sodium acetate trihydrate (ACS grade) was obtained from Laboratoire Mat (Québec, QC, Canada). N-hexane 95% (OPTIMA), Acetonitrile (HPLC grade), Methanol (HPLC grade) was bought from Fisher Scientific (Ottawa, ON, Canada). Potassium hydroxide, ammonium hydroxide and acetic acid were purchased from VWR International (Ville Mont-Royal, QC, Canada) and Ethanol 99% from Commercial Alcohols (Toronto, ON, Canada).

MuSCs culture medium was collected and 10 µl solution of 1% (w/v) BHT and indomethacin (625 µM) per 0.25 ml of sample was added to prevent lipid oxidation and prostaglandin biosynthesis. Bioactive lipids were then extracted by mixing 1 mL of culture medium with 2 mL of 10% MeOH-0.1% acetic acid and 10 µL of deuterated internal standards (25 ng/mL in ethanol). Samples were centrifuged for 3 min at 4000 *x g* before solid phase extractions (SPE). SPE cartridges (Oasis MAX 60 mg/3cc, Waters Corporation Mississauga, Ontario, Canada) were conditioned with methanol and Milli-Q water. Washing steps were made by successive additions of sodium acetate buffer (50 mM, pH 3), N-hexane, ammonium hydroxide (2.5 mM) and lastly with acetonitrile-methanol mixture (8:2 v/v). Bioactive lipids were then eluted with a mixture of 79.2% of acetonitrile, 19.8% methanol and 1% acetic acid and dried under a stream of nitrogen. Samples were reconstituted with 60 mL of 30% acetonitrile-0.01% acetic acid and filtered with Nanoseps centrifugal devices from Pall Corporation (0.2 µm wwPTFE; Pall Biotech – Canada, Mississauga, Ontario, Canada) prior to HPLC injection. The same procedure was used to build a spiked calibration curve.

Bioactive lipid quantification was performed as described previously with a Shimadzu Prominence HPLC (Columbia, MD, USA) coupled to a 3200 QTRAP® mass spectrometer (AB Sciex, Framingham MA, USA)[86,87]. Acquisition was done through Analyst 1.7 (AB Sciex) and the mass spectrometer was operated in multiple-reaction monitoring mode according to transitions shown in Supplementary Table 2. The quantification was achieved by using SCIEX OS 1.7MQ software (AB Sciex).

Single-Cell RNA-Sequencing Analysis

Single-Cell RNA-Sequencing Analysis was performed on the dataset *10X skeletal muscle regeneration scRNA-seq*[35] (accession number GSE138826). The single cell RNA-seq dataset was processed, explored and visualized using Cellenics® community instance (https://scp.biomage.net/) hosted by Biomage (https://biomage.net/) using the app.trailmaker.parsebiosciences.com (Parse Biosciences).

Statistics and reproducibility

All experiments were repeated independently at least twice in the laboratory with similar results. Samples were allocated randomly into experimental groups. The experimenter was blinded to the identity of the sample for data collection and analysis. Data were analyzed using GraphPad Prism (version 9.1.0). Normality test was performed using Shapiro-Wilk. The following statistical tests were performed were appropriate: 2-way paired or unpaired t-test, repeated measure One-Way ANOVA with Uncorrected Fisher's LSD multiple comparisons or 2-way ANOVA with Uncorrected Fisher's LSD multiple comparisons test depending on the experimental setup (details of the test used for each experiment are described in the figure legends). Post-hoc tests were only performed when ANOVA showed a significant difference. Results are reported as means ± standard errors of the mean (SEM). For all tests, the significance value was set at p-value <.05.

Reporting summary

Further information on research design is available in the Nature Portfolio Reporting Summary linked to this article.

Data availability

The scRNAseq data used in this study for the analysis of gene expression at the different time points during muscle regeneration (Fig. 2I, J) are available in the dataset GSE138826. The Bulk RNAseq data used in this study for the analysis of *Gpr37* expression (Supplementary Fig. 6) from myoblasts and macrophages are available from GSE147423 and GSE145243, respectively. The targeted lipidomics data generated in this study are provided in the Source Data file. Source data are provided with this paper.

Code availability

No code was used in this manuscript

References

1. Mauro, A. Satellite cell of skeletal muscle fibers. *J. Biophys. Biochem Cytol.* **9**, 493–495 (1961).
2. Snow, M. H. Myogenic cell formation in regenerating rat skeletal muscle injured by mincing. II. An autoradiographic study. *Anat. Rec.* **188**, 201–217 (1977).
3. Schultz, E., Gibson, M. C. & Champion, T. Satellite cells are mitotically quiescent in mature mouse muscle: an EM and radioautographic study. *J. Exp. Zool.* **206**, 451–456 (1978).
4. Kuang, S., Gillespie, M. A. & Rudnicki, M. A. Niche regulation of muscle satellite cell self-renewal and differentiation. *Cell Stem Cell* **2**, 22–31 (2008).
5. Dort, J., Fabre, P., Molina, T. & Dumont, N. A. Macrophages are key regulators of stem cells during skeletal muscle regeneration and diseases. *Stem Cells Int.* **2019**, 4761427 (2019).
6. Molina, T., Fabre, P. & Dumont, N. A. Fibro-adipogenic progenitors in skeletal muscle homeostasis, regeneration and diseases. *Open Biol.* **11**, 210110 (2021).
7. Zhang, C. et al. Interleukin-6/signal transducer and activator of transcription 3 (STAT3) pathway is essential for macrophage infiltration and myoblast proliferation during muscle regeneration. *J. Biol. Chem.* **288**, 1489–1499 (2013).
8. Arnold, L. et al. Inflammatory monocytes recruited after skeletal muscle injury switch into antiinflammatory macrophages to support myogenesis. *J. Exp. Med.* **204**, 1057–1069 (2007).
9. Dumont, N. & Frenette, J. Macrophages protect against muscle atrophy and promote muscle recovery in vivo and in vitro: a mechanism partly dependent on the insulin-like growth factor-1 signaling molecule. *Am. J. Pathol.* **176**, 2228–2235 (2010).
10. Horsley, V., Jansen, K. M., Mills, S. T. & Pavlath, G. K. IL-4 acts as a myoblast recruitment factor during mammalian muscle growth. *Cell* **113**, 483–494 (2003).
11. Levy, B. D., Clish, C. B., Schmidt, B., Gronert, K. & Serhan, C. N. Lipid mediator class switching during acute inflammation: signals in resolution. *Nat. Immunol.* **2**, 612–619 (2001).
12. Godson, C. et al. Cutting edge: lipoxins rapidly stimulate nonphlogistic phagocytosis of apoptotic neutrophils by monocyte-derived macrophages. *J. Immunol.* **164**, 1663–1667 (2000).
13. Shen, J. et al. Macrophage-mediated 15-lipoxygenase expression protects against atherosclerosis development. *J. Clin. Invest* **98**, 2201–2208 (1996).
14. Munger, K. A. et al. Transfection of rat kidney with human 15-lipoxygenase suppresses inflammation and preserves function in experimental glomerulonephritis. *Proc. Natl Acad. Sci. USA* **96**, 13375–13380 (1999).
15. Kawahara, K., Hohjoh, H., Inazumi, T., Tsuchiya, S. & Sugimoto, Y. Prostaglandin E2-induced inflammation: Relevance of prostaglandin E receptors. *Biochim Biophys. Acta* **1851**, 414–421 (2015).
16. Recchiuti, A. & Serhan, C. N. Pro-resolving lipid mediators (SPMs) and their actions in regulating mirNA in novel resolution circuits in inflammation. *Front Immunol.* **3**, 298 (2012).
17. Basil, M. C. & Levy, B. D. Specialized pro-resolving mediators: endogenous regulators of infection and inflammation. *Nat. Rev. Immunol.* **16**, 51–67 (2016).
18. Serhan, C. N. et al. Reduced inflammation and tissue damage in transgenic rabbits overexpressing 15-lipoxygenase and endogenous anti-inflammatory lipid mediators. *J. Immunol.* **171**, 6856–6865 (2003).
19. Pouliot, M., Clish, C. B., Petasis, N. A., Van Dyke, T. E. & Serhan, C. N. Lipoxin A(4) analogues inhibit leukocyte recruitment to Porphyromonas gingivalis: a role for cyclooxygenase-2 and lipoxins in periodontal disease. *Biochemistry* **39**, 4761–4768 (2000).
20. Spite, M. et al. Resolvin D2 is a potent regulator of leukocytes and controls microbial sepsis. *Nature* **461**, 1287–1291 (2009).
21. Chiang, N. et al. Infection regulates pro-resolving mediators that lower antibiotic requirements. *Nature* **484**, 524–528 (2012).
22. Prescott, D. & McKay, D. M. Aspirin-triggered lipoxin enhances macrophage phagocytosis of bacteria while inhibiting inflammatory cytokine production. *Am. J. Physiol. Gastrointest. Liver Physiol.* **301**, G487–G497 (2011).
23. Lukiw, W. J. et al. A role for docosahexaenoic acid-derived neuroprotectin D1 in neural cell survival and Alzheimer disease. *J. Clin. Invest* **115**, 2774–2783 (2005).
24. Krashia, P. et al. Blunting neuroinflammation with resolvin D1 prevents early pathology in a rat model of Parkinson's disease. *Nat. Commun.* **10**, 3945 (2019).
25. Karp, C. L. et al. Defective lipoxin-mediated anti-inflammatory activity in the cystic fibrosis airway. *Nat. Immunol.* **5**, 388–392 (2004).
26. Chiang, N. & Serhan, C. N. Specialized pro-resolving mediator network: an update on production and actions. *Essays Biochem* **64**, 443–462 (2020).
27. Giannakis, N. et al. Dynamic changes to lipid mediators support transitions among macrophage subtypes during muscle regeneration. *Nat. Immunol.* **20**, 626–636 (2019).
28. Togninalli, M. et al. Machine learning-based classification of dual fluorescence signals reveals muscle stem cell fate transitions in response to regenerative niche factors. *NPJ Regen. Med.* **8**, 4 (2023).
29. Ho, A. T. V. et al. Prostaglandin E2 is essential for efficacious skeletal muscle stem-cell function, augmenting regeneration and strength. *Proc. Natl Acad. Sci. USA* **114**, 6675–6684 (2017).
30. Markworth, J. F. et al. Resolvin D1 supports skeletal myofiber regeneration via actions on myeloid and muscle stem cells. *JCI Insight* **5**, e137713 (2020).
31. Dort, J. et al. Resolvin-D2 targets myogenic cells and improves muscle regeneration in Duchenne muscular dystrophy. *Nat. Commun.* **12**, 6264 (2021).
32. Scher, J. U. & Pillinger, M. H. 15d-PGJ2: the anti-inflammatory prostaglandin?. *Clin. Immunol.* **114**, 100–109 (2005).
33. Miki, Y. et al. Lymphoid tissue phospholipase A2 group IID resolves contact hypersensitivity by driving antiinflammatory lipid mediators. *J. Exp. Med.* **210**, 1217–1234 (2013).
34. Tai, H.-H., Ensor, C. M., Tong, M., Zhou, H. & Yan, F. Prostaglandin catabolizing enzymes. *Prostaglandins Other Lipid Mediat* **68–69**, 483–493 (2002).
35. Oprescu, S. N., Yue, F., Qiu, J., Brito, L. F. & Kuang, S. Temporal dynamics and heterogeneity of cell populations during skeletal muscle regeneration. *iScience* **23**, 100993 (2020).
36. Abrial, C. et al. 15-Lipoxygenases regulate the production of chemokines in human lung macrophages. *Br. J. Pharm.* **172**, 4319–4330 (2015).
37. Chen, Y. et al. Arachidonate 15-lipoxygenase is required for chronic myeloid leukemia stem cell survival. *J. Clin. Invest* **124**, 3847–3862 (2014).
38. Gregus, A. M. et al. Systematic analysis of rat 12/15-lipoxygenase enzymes reveals critical role for spinal eLOX3 hepoxilin synthase activity in inflammatory hyperalgesia. *FASEB J.* **27**, 1939–1949 (2013).
39. Xue, H. et al. The role of ALOX15B in heat stress-induced apoptosis of porcine sertoli cells. *Theriogenology* **185**, 6–15 (2022).
40. Jin, G. et al. Protecting against cerebrovascular injury: contributions of 12/15-lipoxygenase to edema formation after transient focal ischemia. *Stroke* **39**, 2538–2543 (2008).
41. Stenvik Haatveit, Å & Hansen, T. V. The biosynthetic pathways of the protectins. *Prostaglandins Other Lipid Mediat* **169**, 106787 (2023).

42. Serhan, C. N. et al. Anti-inflammatory actions of neuroprotectin D1/protectin D1 and its natural stereoisomers: assignments of dihydroxy-containing docosatrienes. *J. Immunol.* **176**, 1848–1859 (2006).
43. Yoshimoto, Y., Ikemoto-Uezumi, M., Hitachi, K., Fukada, S.-I. & Uezumi, A. Methods for Accurate Assessment of Myofiber Maturity During Skeletal Muscle Regeneration. *Front Cell Dev. Biol.* **8**, 267 (2020).
44. Esper, M. E. et al. Intrinsic muscle stem cell dysfunction contributes to impaired regeneration in the mdx mouse. *J. Cachexia Sarcopenia Muscle* **16**, e13682 (2025).
45. Ren, S. et al. Profound cellular defects attribute to muscular pathogenesis in the rhesus monkey model of Duchenne muscular dystrophy. *Cell* **187**, 6669–6686.e16 (2024).
46. Le Moal, E. et al. Apelin stimulation of the vascular skeletal muscle stem cell niche enhances endogenous repair in dystrophic mice. *Sci. Transl. Med* **16**, eabn8529 (2024).
47. Cardone, N. et al. Myopathologic trajectory in duchenne muscular dystrophy (DMD) reveals lack of regeneration due to senescence in satellite cells. *Acta Neuropathol. Commun.* **11**, 167 (2023).
48. Sugihara, H. et al. Cellular senescence-mediated exacerbation of duchenne muscular dystrophy. *Sci. Rep.* **10**, 16385 (2020).
49. Gosselin, M. et al. Loss of full-length dystrophin expression results in major cell-autonomous abnormalities in proliferating myoblasts. *Elife* **11**, e75521 (2022).
50. Ebert, R. et al. Long-term stimulation of toll-like receptor-2 and −4 upregulates 5-LO and 15-LO-2 expression thereby inducing a lipid mediator shift in human monocyte-derived macrophages. *Biochimica et. Biophysica Acta (BBA) - Mol. Cell Biol. Lipids* **1865**, 158702 (2020).
51. Romano, M., Patruno, S., Pomilio, A. & Recchiuti, A. Proresolving lipid mediators and receptors in stem cell biology: concise review. *Stem Cells Transl. Med* **8**, 992–998 (2019).
52. Cianci, E. et al. Human periodontal stem cells release specialized proresolving mediators and carry immunomodulatory and pro-healing properties regulated by lipoxins. *Stem Cells Transl. Med* **5**, 20–32 (2016).
53. Casati, S. et al. Bioactive lipids in mscs biology: State of the art and role in inflammation. *Int J. Mol. Sci.* **22**, 1481 (2021).
54. Finkensieper, A. et al. The 5-lipoxygenase pathway regulates vasculogenesis in differentiating mouse embryonic stem cells. *Cardiovasc Res* **86**, 37–44 (2010).
55. Yanes, O. et al. Metabolic oxidation regulates embryonic stem cell differentiation. *Nat. Chem. Biol.* **6**, 411–417 (2010).
56. Loynes, C. A. et al. PGE2 production at sites of tissue injury promotes an anti-inflammatory neutrophil phenotype and determines the outcome of inflammation resolution in vivo. *Sci. Adv.* **4**, eaar8320 (2018).
57. Yamane, H., Sugimoto, Y., Tanaka, S. & Ichikawa, A. Prostaglandin E(2) receptors, EP2 and EP4, differentially modulate TNF-alpha and IL-6 production induced by lipopolysaccharide in mouse peritoneal neutrophils. *Biochem Biophys. Res Commun.* **278**, 224–228 (2000).
58. Chen, X.-S., Shelter, J. R., Johnson, E. N. & Funk, C. D. Role of leukotrienes revealed by targeted disruption of the 5-lipoxygenase gene. *Nature* **372**, 179–182 (1994).
59. Collin, M. et al. Reduction of the multiple organ injury and dysfunction caused by endotoxemia in 5-lipoxygenase knockout mice and by the 5-lipoxygenase inhibitor zileuton. *J. Leukoc. Biol.* **76**, 961–970 (2004).
60. Schmid, T. & Brüne, B. Prostanoids and Resolution of Inflammation – Beyond the lipid-mediator class switch. *Front Immunol.* **12**, 714042 (2021).
61. Appel, S. et al. PPAR-gamma agonists inhibit toll-like receptor-mediated activation of dendritic cells via the MAP kinase and NF-kappaB pathways. *Blood* **106**, 3888–3894 (2005).
62. Itoh, K. et al. Transcription factor Nrf2 regulates inflammation by mediating the effect of 15-Deoxy-Δ12,14-Prostaglandin J2. *Mol. Cell Biol.* **24**, 36–45 (2004).
63. Straus, D. S. et al. 15-deoxy-delta 12,14-prostaglandin J2 inhibits multiple steps in the NF-kappa B signaling pathway. *Proc. Natl Acad. Sci. USA* **97**, 4844–4849 (2000).
64. Najar, M. et al. Role of lipocalin-type prostaglandin d synthase in experimental osteoarthritis. *Arthritis Rheumatol.* **72**, 1524–1533 (2020).
65. Wu, D. et al. Novel biphasic role of resolvin D1 on expression of cyclooxygenase-2 in lipopolysaccharide-stimulated lung fibroblasts is partly through PI3K/AKT and ERK2 pathways. *Mediators Inflamm.* **2013**, 964012 (2013).
66. Le Grand, F., Jones, A. E., Seale, V., Scimè, A. & Rudnicki, M. A. Wnt7a activates the planar cell polarity pathway to drive the symmetric expansion of satellite stem cells. *Cell Stem Cell* **4**, 535–547 (2009).
67. Sharma, B. et al. Leukocyte-type 12/15-lipoxygenase is essential for timely inflammation-resolution and effective tissue regeneration following skeletal muscle injury. *bioRxiv [Preprint].* https://doi.org/10.1101/2025.05.13.653766 (2025).
68. Bhattacharya, A. et al. Genetic ablation of 12/15-lipoxygenase but not 5-lipoxygenase protects against denervation-induced muscle atrophy. *Free Radic. Biol. Med.* **67**, 30–40 (2014).
69. Li, J. & Johnson, S. E. ERK2 is required for efficient terminal differentiation of skeletal myoblasts. *Biochem Biophys. Res Commun.* **345**, 1425–1433 (2006).
70. Li, X. et al. Extracellular signal-regulated kinase 1/2 mitogen-activated protein kinase pathway is involved in inhibition of myogenic differentiation of myoblasts by hypoxia. *Exp. Physiol.* **97**, 257–264 (2012).
71. White, P. J. et al. Protectin DX alleviates insulin resistance by activating a myokine-liver glucoregulatory axis. *Nat. Med.* **20**, 664–669 (2014).
72. Markworth, J. F. et al. Metabolipidomic profiling reveals an age-related deficiency of skeletal muscle pro-resolving mediators that contributes to maladaptive tissue remodeling. *Aging Cell* **20**, e13393 (2021).
73. Duffield, J. S. et al. Resolvin D series and protectin D1 mitigate acute kidney injury. *J. Immunol.* **177**, 5902–5911 (2006).
74. Park, K.-D. et al. Protectin D1 reduces imiquimod-induced psoriasiform skin inflammation. *Int Immunopharmacol.* **98**, 107883 (2021).
75. Levy, B. D. et al. Protectin D1 is generated in asthma and dampens airway inflammation and hyperresponsiveness. *J. Immunol.* **178**, 496–502 (2007).
76. Dort, J., Orfi, Z., Fiscaletti, M., Campeau, P. M. & Dumont, N. A. Gpr18 agonist dampens inflammation, enhances myogenesis, and restores muscle function in models of Duchenne muscular dystrophy. *Front Cell Dev Biol.* **11**, 1187253 (2023).
77. Tavakoli, S. et al. Transplantation-based screen identifies inducers of muscle progenitor cell engraftment across vertebrate species. *Cell Rep.* **42**, 112365 (2023).
78. Ganassi, M., Muntoni, F. & Zammit, P. S. Defining and identifying satellite cell-opathies within muscular dystrophies and myopathies. *Exp. Cell Res.* **411**, 112906 (2022).
79. Ganassi, M. & Zammit, P. S. Involvement of muscle satellite cell dysfunction in neuromuscular disorders: Expanding the portfolio of satellite cell-opathies. *Eur. J. Transl. Myol.* **32**, 10064 (2022).
80. Conte, T. C. et al. Clearance of defective muscle stem cells by senolytics restores myogenesis in myotonic dystrophy type 1. *Nat. Commun.* **14**, 4033 (2023).
81. Zhang, S., Ye, J. & Dong, G. Neuroprotective effect of baicalein on hydrogen peroxide-mediated oxidative stress and mitochondrial dysfunction in PC12 cells. *J. Mol. Neurosci.* **40**, 311–320 (2010).

82. Fabre, P., Molina, T., Orfi, Z. & Dumont, N. A. Assessment of muscle function following hipsc-derived myoblast transplantation in dystrophic mice. *Curr. Protoc.* **2**, e356 (2022).
83. Dumont, N. A. & Rudnicki, M. A. Characterizing satellite cells and myogenic progenitors during skeletal muscle regeneration. *Methods Mol. Biol.* **1560**, 179–188 (2017).
84. Lau, Y. S., Xu, L., Gao, Y. & Han, R. Automated muscle histopathology analysis using cellprofiler. *Skelet. Muscle* **8**, 32 (2018).
85. Babcock, L. W., Hanna, A. D., Agha, N. H. & Hamilton, S. L. MyoSight-semi-automated image analysis of skeletal muscle cross sections. *Skelet. Muscle* **10**, 33 (2020).
86. Bilodeau, J.-F. et al. Long chain omega-3 fatty acids and their oxidized metabolites are associated with reduced prostate tumor growth. *Prostaglandins Leukot. Ess. Fat. Acids* **164**, 102215 (2021).
87. Rieger, L. et al. Transcriptomic and lipidomic profiling reveals distinct bioactive lipid signatures in slow and fast muscles and highlights the role of resolvin-D2 in fiber type determination during myogenesis. *FASEB J.* **38**, e70250 (2024).
88. Fabre, P. https://BioRender.com/fihrzfx (2025)
89. Fabre, P. https://BioRender.com/p47v568 (2025).
90. Fabre, P. https://BioRender.com/u95r894 (2025).
91. Fabre, P. https://BioRender.com/x26a839 (2025).
92. Fabre, P. https://BioRender.com/f07o565 (2025).
93. Fabre, P. https://BioRender.com/r52v373 (2025).
94. Fabre, P. https://BioRender.com/g09q327 (2025).

Acknowledgements

We thank Sonja Lespérance for animal husbandry. P.F., T.M., and I.M. were supported by a fellowship from the Fonds de Recherche du Québec - Santé (FRQS). A.D. was supported by a fellowship from the Fonds de Recherche du Québec - Nature et Technologies (FRQNT). G.G.G. was supported by a fellowship from Natural Sciences and Engineering Research Council of Canada (NSERC). J.D. was supported by the Muscular Dystrophy Association. E.D. was supported by FRQS Junior 1 award (#31186) and N.A.D. was supported by a FRQS Junior-2 award (#296512) and Canada Research Chair tier 2 (CRC-2024-00025). This project was supported by research grants to N.D. from NSERC (#RGPIN-2018-05979) and Canadian Institutes of Health Research (#PJT-156408 and PJT-186202). This study was supported by the Quebec Cell, Tissue and Gene Therapy Network –ThéCell (a thematic network supported by the FRQS).

Author contributions

N.A.D. and P.F. conceived the project and designed the experiments. P.F., T.M., J.L., K.G., G.G.G., A.D., I.M., O.P., and J.D. performed experiments, collected, and analyzed data. P.F. and N.A.D. wrote the manuscript. J.F.B. designed, managed, and supervised the lipidomics analyses, E.D. contributed to the human data collection and analysis, and N.A.D. managed and supervised the overall project. All authors carefully reviewed and provided critical insights into the manuscript.

Competing interests

The authors declare no competing interests.

Additional information

Supplementary information The online version contains supplementary material available at https://doi.org/10.1038/s41467-025-60586-8.

Correspondence and requests for materials should be addressed to Nicolas A. Dumont.

Peer review information *Nature Communications* thanks the anonymous reviewers for their contribution to the peer review of this work. A peer review file is available.

Reprints and permissions information is available at http://www.nature.com/reprints

Publisher's note Springer Nature remains neutral with regard to jurisdictional claims in published maps and institutional affiliations.

Open Access This article is licensed under a Creative Commons Attribution-NonCommercial-NoDerivatives 4.0 International License, which permits any non-commercial use, sharing, distribution and reproduction in any medium or format, as long as you give appropriate credit to the original author(s) and the source, provide a link to the Creative Commons licence, and indicate if you modified the licensed material. You do not have permission under this licence to share adapted material derived from this article or parts of it. The images or other third party material in this article are included in the article's Creative Commons licence, unless indicated otherwise in a credit line to the material. If material is not included in the article's Creative Commons licence and your intended use is not permitted by statutory regulation or exceeds the permitted use, you will need to obtain permission directly from the copyright holder. To view a copy of this licence, visit http://creativecommons.org/licenses/by-nc-nd/4.0/.

© The Author(s) 2025